

Galaxy Morphologies at Cosmic Noon with *JWST*: A Foundation for Exploring Gas Transport with Bars and Spiral Arms

Juan M. Espejo Salcedo^{1*}, Stavros Pastras^{1,2}, Josef Vácha³, Claudia Pulsoni¹, Reinhard Genzel¹, N. M. Förster Schreiber¹, Jean-Baptiste Jolly¹, Capucine Barfety¹, Jianhang Chen¹, Giulia Tozzi¹, Daizhong Liu^{1,4}, Lilian Lee¹, Stijn Wuyts⁵, Linda Tacconi¹, Ric Davies¹, Hannah Übler¹, Dieter Lutz¹, Emily Wisnioski^{6,7}, Jinyi Shangguan^{1,8}, Minju Lee^{9,10}, Sedona H. Price¹¹, Frank Eisenhauer¹, Alvio Renzini¹², Amit Nestor Shachar¹³, and Rodrigo Herrera-Camus¹⁴

¹ Max-Planck-Institut für extraterrestrische Physik (MPE), Giessenbachstraße 1., 85748 Garching, Germany

² Max-Planck-Institut für Astrophysik (MPA), Karl-Schwarzschild-Str. 1, 85748, Garching, Germany

³ Department of Physics, University of Oxford, Clarendon Laboratory, Parks Road, OX1 3PU Oxford, UK

⁴ Purple Mountain Observatory, Chinese Academy of Sciences, 10 Yuanhua Road, Nanjing 210023, China

⁵ Department of Physics, University of Bath, Claverton Down, Bath BA2 7AY, UK

⁶ Research School of Astronomy and Astrophysics, Australian National University, Weston Creek, ACT 2611, Australia

⁷ ARC Centre of Excellence for All Sky Astrophysics in 3 Dimensions (ASTRO 3D), Canberra, ACT 2611, Australia

⁸ Kavli Institute for Astronomy and Astrophysics, Peking University, Beijing 100871, People's Republic of China

⁹ Cosmic Dawn Center (DAWN), Denmark

¹⁰ DTU-Space, Technical University of Denmark, Elektrovej 327, DK2800 Kgs. Lyngby, Denmark

¹¹ Department of Physics and Astronomy and PITT PACC, University of Pittsburgh, Pittsburgh, PA 15260, USA

¹² Osservatorio Astronomico di Padova, Vicolo dell'Osservatorio 5, Padova I-35122, Italy

¹³ School of Physics and Astronomy, Tel Aviv University, Tel Aviv 69978, Israel

¹⁴ Universidad de Concepción, Víctor Lamas 1290, Barrio Universitario, Concepción, Chile

Received ...; accepted ...

ABSTRACT

How radial flows shape galaxy structure and evolution remains an open question. Internal drivers of such flows, such as bars and spiral arms, known to mediate gas flows in the local Universe, are now observable at high redshift thanks to *JWST*'s unobscured view. We investigate the morphology of massive star-forming galaxies at $0.8 < z < 1.3$ and $2.0 < z < 2.5$, epochs marking the peak and decline of cosmic star formation, both well-covered by kinematic surveys. Using *JWST*/NIRCam imaging, we visually classify 1,451 galaxies, identify non-axisymmetric features, count the number of spiral arms, analyze non-parametric morphological indicators and study the dynamical support of the sample covered by kinematics (10% of the sample) as measured via v/σ . Disk galaxies dominate the sample (82%), with 48% exhibiting spiral structure and 11% hosting bars. Both fractions decline with redshift, consistent with previous studies. The proportion of two- and three-armed spirals remains largely unchanged across redshift, with roughly two-thirds showing two arms and one-third showing three arms in both bins. Notably, we find a higher incidence of three-armed spirals than reported in the local Universe, suggesting a mild evolution in spiral arm multiplicity. Non-parametric morphological metrics strongly correlate with stellar mass but show no significant redshift evolution. Finally, kinematic analysis reveals a strong correlation between disk morphology and rotational support, with most disks exhibiting $v/\sigma > 3$ and median values of $v/\sigma > 7$ for spirals and $v/\sigma > 5$ for barred galaxies. This study establishes a population-wide framework for linking galaxy morphology and dynamics at cosmic noon, providing a key reference for future studies on the role of detailed structural features in galaxy evolution.

Key words. galaxies: disks – galaxies: morphology – galaxies: evolution

1. Introduction

A fundamental question in galaxy evolution is how early star-forming galaxies assembled the well-ordered structures seen in the present-day Universe. While early morphological studies suggested that high-redshift galaxies were highly irregular and dynamically unstable, kinematic surveys have since revealed that disk-like rotation is widespread at cosmic noon ($1 < z < 3$) (e.g., Förster Schreiber et al. 2009; Law et al. 2009; Wisnioski et al. 2015; Stott et al. 2016; Simons et al. 2017; Harrison et al. 2017; Übler et al. 2019). Integral field spectroscopy has consistently shown that a large fraction of star-forming galaxies at these epochs exhibit strong rotational support, often with velocity dis-

persions lower than expected for turbulent, irregular morphologies. These findings challenged the prevailing view based on *HST* imaging, which primarily identified galaxies with clumpy, chaotic structures (e.g., Abraham et al. 1996; Conselice et al. 2000; Jogee et al. 2004; Lotz et al. 2006; Elmegreen et al. 2007; Sheth et al. 2008).

With the advent of the *HST* Wide Field Camera 3 (WFC3) and near-infrared imaging, deeper surveys began to reveal a growing number of galaxies with more regular morphologies. By tracing rest-frame optical emission, these observations identified an increasing fraction of disk-like systems and even reported the presence of spiral arms and bars in some of them—though the full prevalence of disks and their substructures remained uncertain due to resolution and surface brightness limitations (e.g.,

* e-mail: jespejo@mpe.mpg.de

Wuyts et al. 2011b; van der Wel et al. 2014; Morishita et al. 2014; Guo et al. 2015; Kartaltepe et al. 2015).

The arrival of *JWST* has dramatically transformed our ability to study galaxy structure at high redshift, offering a combination of longer wavelengths, increased depth, and unprecedented resolution. Recent studies leveraging *JWST* NIRCcam imaging consistently reveal a high fraction of disk galaxies at and beyond cosmic noon (e.g., Jacobs et al. 2023; Ferreira et al. 2023; Kartaltepe et al. 2023; Liu et al. 2023; Nelson et al. 2023; Huertas-Company et al. 2024; Lee et al. 2024; Tohill et al. 2024; Pandya et al. 2024). Additionally, some studies provide clear evidence of spiral arms and bars (e.g., Costantin et al. 2023; Ferreira et al. 2023; Guo et al. 2023; Kuhn et al. 2024; Le Conte et al. 2024; Chugunov et al. 2025). Thus, many galaxies that once appeared irregular or clumpy in *HST* imaging are now recognized as well-ordered disks, with some exhibiting prominent non-axisymmetric features, reaffirming the prevalence of disk from kinematics studies in the pre-*JWST* time and the now consistent disk fractions inferred from morphology and kinematics-based studies.

Beyond their prevalence, these non-symmetric morphological features are key agents of secular evolution, regulating gas flows and star formation within galaxies. In the local Universe, bars and spiral arms are known to redistribute angular momentum and funnel gas toward galaxy centres, often fueling central star formation and bulge growth. As demonstrated by Yu et al. (2022) with the EDGE-CALIFA survey of local galaxies, both spiral arms and bars efficiently channel gas inward, leading to higher central gas concentrations and elevated star formation rates.

If these mechanisms were already at play at cosmic noon, they could have profound implications for the early buildup of galaxy structure. Recent kinematic studies have uncovered evidence for rapid radial inflows in high-redshift main-sequence disks (e.g., Genzel et al. 2023, Pastras et al. in prep), suggesting that these processes may have been even more pronounced in the past. These findings contradict earlier expectations that non-axisymmetric structures like spiral arms and bars would be short-lived in gas-rich, turbulent environments (e.g., Genzel et al. 2008; Ceverino et al. 2010; Bournaud et al. 2011). Instead, they suggest that such features were not only prevalent but also played a fundamental role in shaping galaxy evolution throughout cosmic time. Given these advancements, establishing a direct connection between morphology and kinematics is crucial for understanding how high-redshift disks evolve and whether non-axisymmetric features are primary drivers of internal gas flows and structural transformation.

In this study, we exploit *JWST* NIRCcam imaging to investigate the morphologies of massive main-sequence galaxies at $1 < z < 3$, focusing on key redshift bins that correspond to epochs of peak and declining cosmic star formation activity (e.g., Madau & Dickinson 2014; Förster Schreiber & Wuyts 2020). One bin corresponds to an epoch of peak cosmic star formation activity ($2.0 < z < 2.5$), and the other bin represents a later period of declining star formation rates ($0.8 < z < 1.3$). These bins also match redshift ranges for which $H\alpha$ is observable from the ground, and large $H\alpha$ kinematics samples are available.

Our goal is to establish a robust morphological foundation for interpreting the growing body of kinematic measurements from near-infrared integral field spectroscopy and millimetre/submillimetre observations. Specifically, our sample selection aligns with that of major spectroscopic surveys such as KMOS^{3D}, SINS, KROSS, NOEMA-3D and PHIBSS, thus enabling the connections between the morphological and kine-

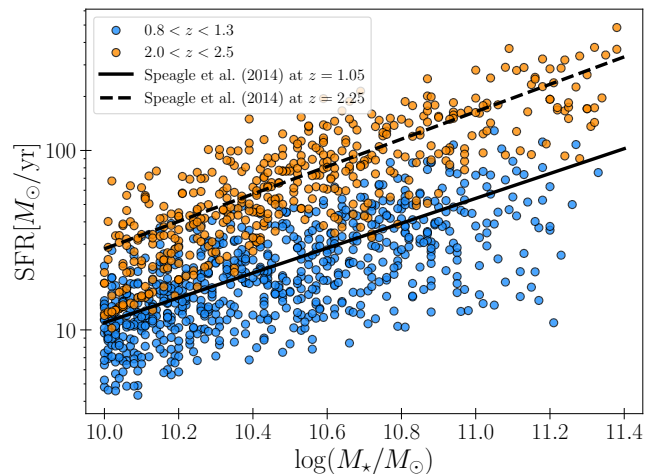


Fig. 1: Star-formation rate (SFR) vs stellar mass M_* for the selected sample, with the Speagle et al. (2014) relations for the mid-points of the redshift bins $z = 1.05$ and $z = 2.25$.

matic analyses. By providing a comprehensive visual classification of galaxy structure (including disks, bars, and spiral arms), this work serves as a key reference for future studies aiming to investigate the connections between morphology, gas transport and secular evolution. Additionally, we complement our visual classifications with quantitative (non-parametric) morphological metrics, leveraging well-established statistical methods to characterize galaxy structure and to systematically link morphology and dynamics at cosmic noon.

In §2, we describe the sample selection, followed by a discussion of the imaging data, its corresponding data reduction methods, and the assembly of the kinematic sample used in this study. §3 presents the overall morphological properties of the sample, detailing the visual classification scheme, general classification results, and the identification of bars and spiral structures. §4 examines the evolution of these morphological features with redshift and compares our findings with previous studies. In §5, we perform a quantitative analysis of galaxy morphology, exploring non-parametric structural indicators and their relationship to the visual classifications. §6 investigates the connection between morphology and kinematics, discussing the implications for galaxy evolution. Finally, §7 summarizes the key findings of this work. Additional details, including discussions of observational limitations, preparations for the morphological analysis, and a description of the methodology used to separate galaxy morphologies based on structural metrics, and comparisons with *HST* photometry are provided in Appendices A-D.

We adopt a Λ CDM cosmology with $\Omega_m = 0.3$, $\Omega_\Lambda = 0.7$, and $H_0 = 70 \text{ km s}^{-1} \text{ Mpc}^{-1}$. In this framework, one arcsecond corresponds to 8.1 kpc at $z = 1.05$ and 8.24 kpc at $z = 2.25$, which are the mid-points of the two chosen redshift bins.

2. Sample

2.1. NIRCcam imaging

To investigate morphological evolution at cosmic noon, we focus on two epochs corresponding to $0.8 < z < 1.3$ and $2.0 < z < 2.5$. Since star-forming galaxies dominate the population at these epochs, we apply selection criteria targeting massive star-forming galaxies with star formation rates (SFR) within 0.4 dex of the star formation main sequence (MS), as parametrized by

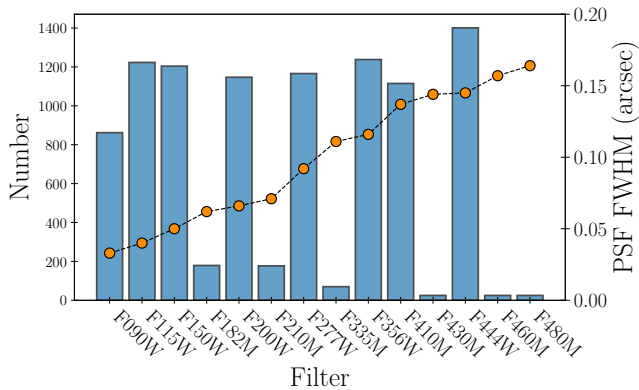


Fig. 2: Number of galaxies observed in each filter. The most frequently observed filter combination—F090W, F115W, F150W, F200W, F277W, F356W, F410M, and F444W—is shared by 739 galaxies (51% of the sample), meaning these galaxies were observed in all these filters. The orange dots indicate the empirical PSF FWHM in each filter. To reduce overcrowding, we omit F250M and F300M, which contain only 10 galaxies each.

Whitaker et al. (2014), i.e., $\log(\text{SFR}/\text{SFR}_{\text{MS}}) = [-0.4, 0.4]$. Additionally, we choose masses within $\log(M_{\star}/M_{\odot}) = [10.0, 11.4]$, and sizes in the range $r_{\text{eff}} \text{ (arcsec)} = [0.2, 1.0]$. The criteria are designed to represent the bulk of typical star-forming galaxies over a mass range large enough to explore trends with stellar mass.

The quantities used in this selection are derived from the 3D-HST catalogue by Momcheva et al. (2016) (see also Brammer et al. 2012; Skelton et al. 2014), which serves as the parent sample for this study and global galaxy properties such as stellar mass and star formation rates are derived following the prescriptions by Wuyts et al. (2011a). Figure 1 provides a visualization of the sample distribution in the SFR vs M_{\star} plane across the two redshift bins.

Building on this 3D-HST-based selection, we collected available NIRCcam imaging from public data releases of major *JWST* surveys, specifically JADES (Finkelstein et al. 2023) and CEERS (Bagley et al. 2023). These data span the five CANDELS fields (Koekemoer et al. (2011); Grogin et al. (2011)): the UKIDSS Ultra Deep Survey (UDS; Lawrence et al. 2007; Cirasuolo et al. 2007), the Extended Groth Strip (EGS; Davis et al. 2007), the Cosmic Evolution Survey (COSMOS; Scoville et al. 2007; Koekemoer et al. 2007), and the Great Observatories Origins Deep Survey (GOODS) North and South (Giavalisco et al. 2004). Table 1 provides an overview of the sample sizes in each of the CANDELS fields.

For each galaxy, we use a uniform pixel scale of 0.025 arcsec per pixel and retrieve the NIRCcam images across all available filters covering the range $0.9 \mu\text{m} < \lambda < 4.8 \mu\text{m}$. Among the used filters, 7 are broadband (F090W, F115W, F150W, F200W, F277W, F356W, and F444W), and 9 are mediumband (F182M, F210M, F250M, F300M, F335M, F410M, F430M, F460M, and F480M). The most commonly available filter combination in our dataset consists of eight filters—F090W, F115W, F150W, F200W, F277W, F356W, F410M, and F444W—and covers 739 galaxies, making it particularly useful for assessing filter dependence in morphological measurements. Our sample consists of a total of 1,451 galaxies (9877 NIRCcam images in total), with 811 and 640 in the low- and high-redshift bins, respectively. Figure 2 presents the number of galaxies observed in each filter along

Table 1: Distribution of the number of galaxies over the CANDELS deep fields and redshift bins.

Field	Number	$0.8 < z < 1.3$	$2.0 < z < 2.5$
UDS	399	199	200
EGS	298	165	133
COSMOS	399	243	156
GOODS-South	155	83	72
GOODS-North	200	121	79
All fields	1,451	811	640

with the corresponding empirical PSF size in arcseconds¹. As shown by Lee et al. (2024), using empirically derived PSFs from field stars in different deep fields has a negligible impact on the inferred morphological fractions across all fields and introduces only minor systematic biases in Sérsic indices.

2.2. Reduction of imaging data

We evaluated two distinct data reduction approaches: the public releases from the DAWN *JWST* Archive² reduction (v7.0 + v7.1) and JADES³ (Eisenstein et al. 2023) (v2.0) as well as our custom reduction pipeline. The DAWN Archive provides high-quality reductions of *JWST* NIRCcam data using the *grizli* reduction framework (Brammer 2025), which includes baseline calibrations, astrometric alignment using *DrizzlePac*, and background subtraction optimized for faint structure preservation and noise minimization. The JADES reduction products, while also high-quality, place greater emphasis on precise background modelling and outlier rejection via median mosaics, whereas *Grizli* (DAWN) applies global sky corrections and sigma-clipping during stacking. For astrometric alignment, JADES employs MONTAGE3, which offers precise registration across multiple exposures, differing from the *DrizzlePac*-based approach used in DAWN.

In parallel, we developed a custom reduction pipeline tailored to the specific requirements of our analysis. The reduction follows the standard *JWST* image processing stages⁴: *i*) converting detector volt signals into rates of units of data numbers per second (DN/s); *ii*) calibrating rates into flux densities and assigning world coordinates; and *iii*) creating mosaic images from individual exposures while median-clipping outlier pixels. Building on previous studies (e.g., Bagley et al. 2023; M. Franco et al. in prep.), we also: *i*) improved removal of NIRCcam imaging $1/f$ noise by detecting and subtracting horizontal and vertical stripes; *ii*) enhanced removal of “snowballs” and “claws” through a combination of manual masking and template fitting, using the NIRCcam team’s templates⁵; *iii*) improved world coordinate alignment (astrometry correction) by first detecting bright

¹ Empirical PSF sizes used in this work are taken from <https://jwst-docs.stsci.edu/jwst-near-infrared-camera>

² <https://dawn-cph.github.io/dja/>

³ <https://archive.stsci.edu/hlsp/jades>

⁴ <https://jwst-docs.stsci.edu/jwst-science-calibration-pipeline/stages-of-jwst-data-processing>

⁵ <https://jwst-docs.stsci.edu/depreciated-jdox-articles/nircam-claws-and-wisps>. The latest templates were released recently (<https://www.stsci.edu/contents/news/jwst/2024/new-nircam-wisp-templates-are-now-available>), but as our visually inspected targets are unaffected by claws, we did not update our reduction with the latest templates.

Kinematics of the 155 overlapping galaxies (10% coverage)

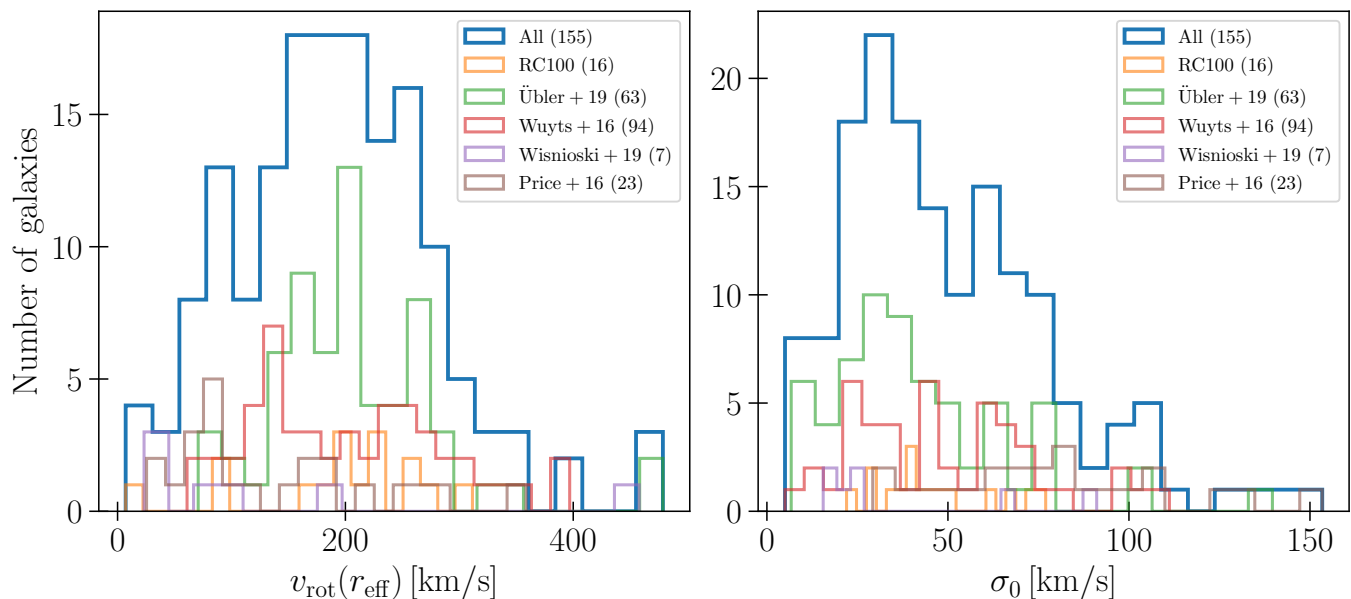


Fig. 3: Histograms showing the distribution of rotational velocity $v_{\text{rot}}(r_{\text{eff}})$ (left) and velocity dispersion σ_0 (right) for different galaxy samples including the RC100 (Nestor Shachar et al. 2023), and those from Übler et al. (2019), Wuyts et al. (2016), Wisnioski et al. (2019), and Price et al. (2016). The legend indicates the datasets included, with the number of galaxies in each sample shown in parentheses. The “All” sample (blue) represents the full dataset, while other colours correspond to specific subsamples from various studies.

unsaturated stars/galaxies using *SEXTRACTOR* (Bertin & Arnouts 1996) and then cross-matching them with 3D-HST reference galaxy catalogues, ensuring alignment of *JWST* images with 3D-HST images; *iv*) additional flat background subtraction at the end of stage 2 using the Python *PHOTUTILS* package before mosaicking to homogenize the mosaic background.

All scripts and manual mask regions are publicly available on GitHub⁶. We processed the imaging data as soon as they became available in the *JWST* MAST archive from various programs, frequently updating the Calibration Reference Data System (CRDS) and *JWST* pipeline versions. For this study, the final products used for the morphology analysis were processed using CRDS calibration versions 1023–1130 and the *JWST* pipeline versions 1.9.0–1.11.4. The final images were produced with a pixel scale of 25 mas, aligned with North up, to facilitate the morphological analysis.

Prioritizing minimal noise, optimal background subtraction, and consistent PSF characteristics, we primarily adopted the DAWN reductions, which accounted for the majority of our sample ($\approx 96\%$). The JADES reductions were used for a small fraction of galaxies ($\approx 2\%$), while our custom reductions were employed in a few cases ($\approx 2\%$). Importantly, all three reduction pipelines produced high-quality data, ensuring that our final sample remained uniform and unaffected by these choices. To maintain consistency across filters, we ensured that all images for a given galaxy originated from the same reduction pipeline.

2.3. Kinematics sample

To trace the dynamical evolution of galaxies at the epochs probed in this study, we also examine the interplay between morpholog-

ical features observed in the *JWST* NIRC*am* images and available kinematic measurements, specifically the v/σ ratio, which provides crucial insights into each galaxy’s dynamical state. To compile the kinematic data, we use measurements from well-established surveys and studies.

The KMOS^{3D} survey (Wisnioski et al. 2015) is the largest and deepest IFU survey in the deep fields, covering a redshift range of $z \sim 0.6 - 2.6$. This survey has provided key insights into the kinematic properties of star-forming galaxies across cosmic time, utilizing high-resolution H α emission line maps obtained with KMOS (K-band Multi-Object Spectrograph) on the VLT. Multiple studies have explored the kinematics of these galaxies using a variety of techniques, including disk modelling, kinematic classification, and dynamical mass estimates (e.g., Burkert et al. 2016; Wuyts et al. 2016; Genzel et al. 2017; Übler et al. 2017; Lang et al. 2017; Übler et al. 2018; Wisnioski et al. 2019; Förster Schreiber et al. 2019). These analyses have provided critical constraints on the evolution of angular momentum, velocity dispersion, and the transition between rotation- and dispersion-dominated systems. Beyond KMOS^{3D}, we incorporate high-resolution kinematic measurements for 100 galaxies (RC100) based on H α and CO tracers from Nestor Shachar et al. (2023), as well as slit-spectroscopy kinematics from Price et al. (2016). For galaxies with multiple kinematic measurements, we prioritize data sources based on methodological advancements and data quality, following this order: RC100 (Nestor Shachar et al. 2023), followed by KMOS^{3D}-based studies (Übler et al. 2019; Wuyts et al. 2016; Wisnioski et al. 2019), and finally, the slit-spectroscopic MOSDEF survey (Price et al. 2016).

We found an overlap of 155 galaxies with existing measurements of velocity and velocity dispersion. For consistency, we adopt a standardized approach, using the rotation velocity at one effective radius, $v_{\text{rot}}(r_{\text{eff}})$, and assumed a radially constant intrinsic

⁶ <https://github.com/1054/Crab.Toolkit.JWST>

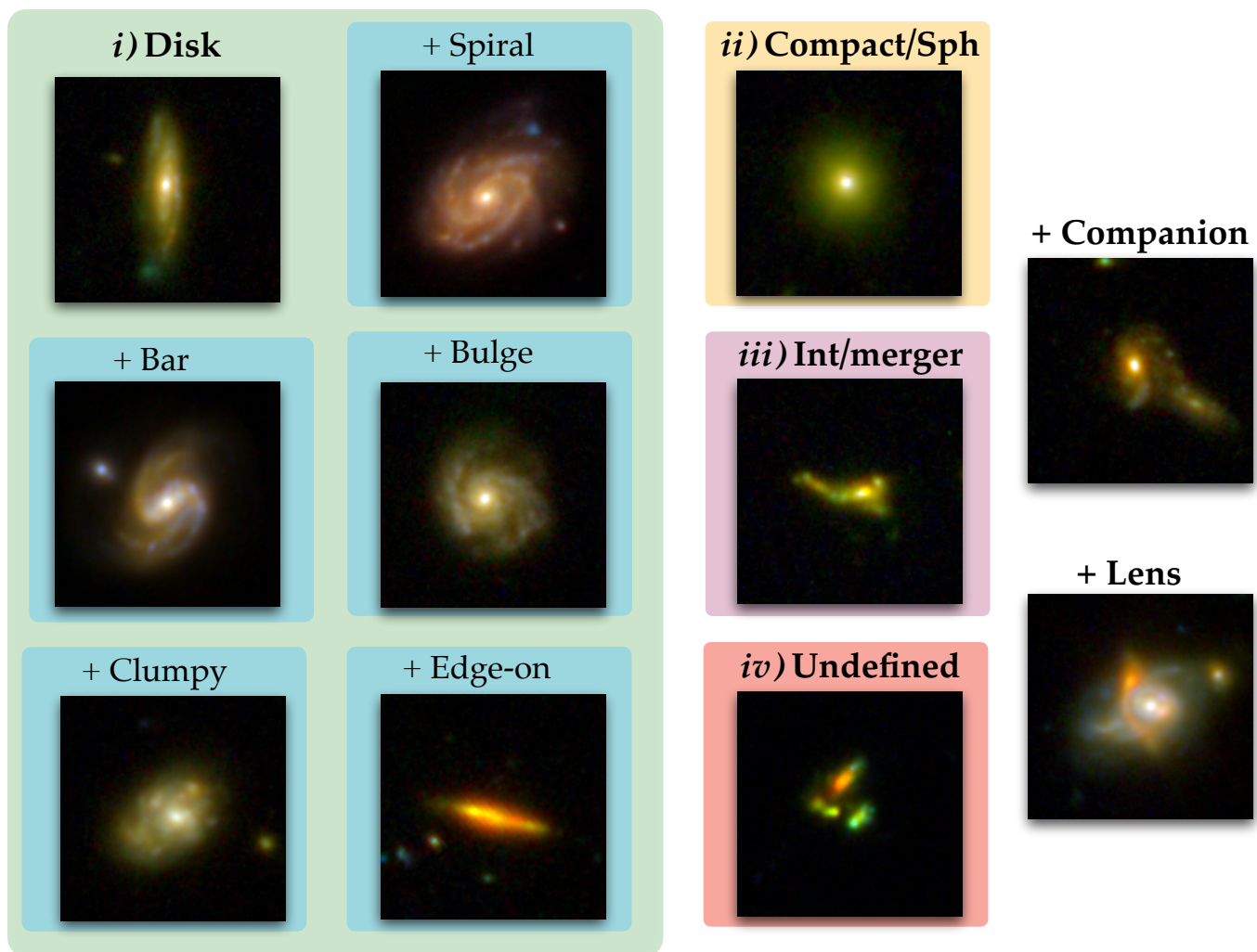


Fig. 4: Classification scheme used in the visual classification, with examples from the galaxy sample analyzed in this study. The green, yellow, purple and red coloured boxes indicate the four main categories: Disk, Compact/Spheroidal, Interacting/Merger, and Undefined. The “+ Companion” and “+ Lens” classifications are non-mutually exclusive, meaning a galaxy could belong to any of the main categories while also being identified to have a companion or a lensed system. The blue squares inside the disk category correspond to the five non-exclusive morphological features that a disk galaxy can have.

sic disk velocity dispersion σ_0 , corrected for observational effects, such as beam smearing, as derived from modelling. The detailed measurement adjustments are outlined as follows:

- For RC100 (Nestor Shachar et al. 2023), where we included 16 out of their 100 galaxies, we used reported circular velocities and applied the following correction to obtain $v_{\text{rot}}(r_{\text{eff}})$:

$$v_{\text{rot}}^2(r) = v_{\text{circ}}^2(r) - 3.36 \left(\frac{r}{r_{\text{eff}}} \right) \sigma_0^2 \quad (1)$$

- In Übler et al. (2019), we identified an overlap of 71 galaxies from their sample of 187; however, based on our prioritization, and since some of these are already in the RC100 sample, we included 63. The study reported values for $v_{\text{rot}}(r = 1.38r_{\text{eff}})$, which we adjusted to $v_{\text{rot}}(r_{\text{eff}})$ using rotation curve models for a thick disk as described by Noordermeer (2008).
- For Wuyts et al. (2016), out of a sample of 240, we used 50 galaxies based on prioritization criteria.
- In Wisnioski et al. (2019), from a total number of 745, we identified 7 more overlapping galaxies.

- Lastly, for Price et al. (2020) (MOSDEF), we identified 26 overlapping galaxies from their full sample of 1,717, of which we used 23. Since these measurements were based on slit spectroscopy with the MOSFIRE instrument, the slits could not be precisely aligned with the galaxies’ major axes. The sample of 23 used here is restricted to objects that are spatially resolved (under seeing-limited conditions), with reasonable alignment between slit and galaxy major axes ($|\Delta\text{PA}| \leq 45^\circ$), and have detected rotation signatures (within the uncertainties). We note that this work used an arctan parametric fit to derive the rotation velocity profile, differing from the parametric fits used in other surveys. Moreover, as the exact kinematic major axes were unknown, the modelling assumed the morphological and kinematic axes were the same, introducing potential systematics. However, given the small sample size, any such effect is unlikely to have a significant impact on our overall analysis.

An overview of the distributions of velocities and velocity dispersions is shown in Figure 3.

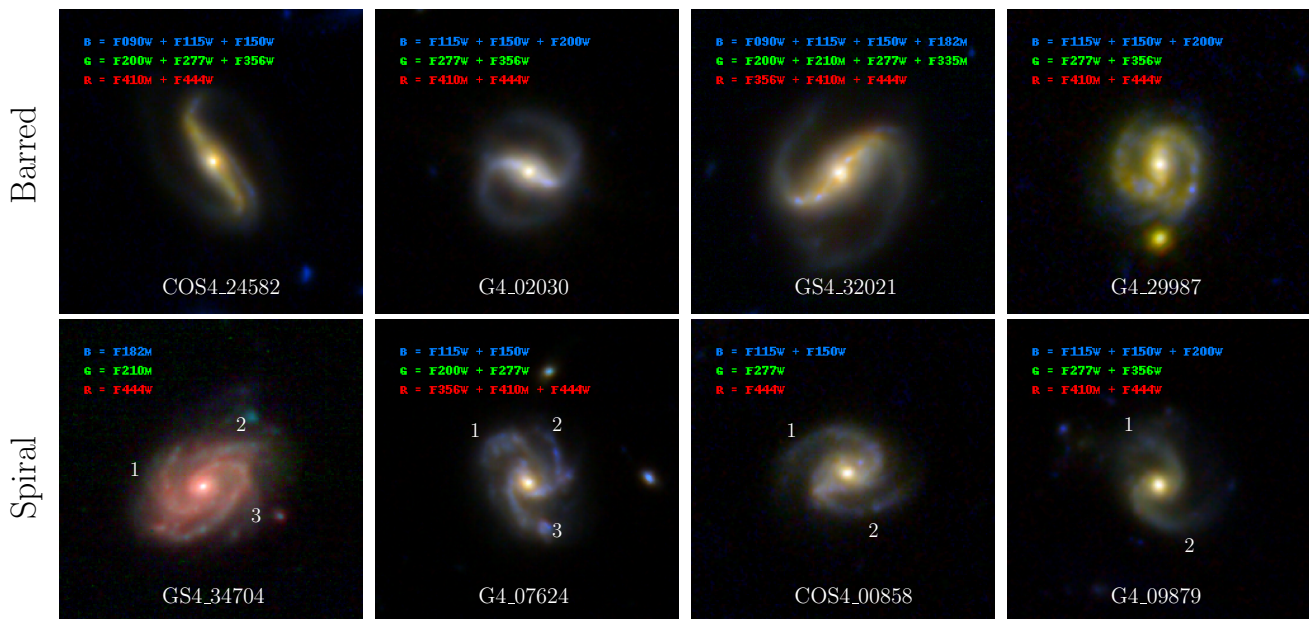


Fig. 5: Example colour composite images of galaxies classified as barred (top row) and spiral (bottom row). These categories are not mutually exclusive, as many barred galaxies also exhibit clear spiral arms. The filters used to create each composite image are labelled in the top left corner of each panel. The numbers in the bottom row indicate the number of spiral arms identified in the visual classification. The full mosaics of the barred and spiral galaxies can be found in the following two links: bars and spirals.

3. Visual classifications of morphology

3.1. Classification scheme

To prepare the *JWST* NIRC*am* imaging for analysis, we first fit the images with a single Sérsic profile using *GALFIT* (Peng et al. 2002, 2010) for each stamp. Initial source detection relied on segmentation maps, which provided preliminary inputs for the *GALFIT* routine. Following this, six of the authors of this work (J.M.E.S, C.B, S.P, C.P, J.C, J-B.J) visually classified all the galaxies in the sample. For increased robustness, the morphological classification process incorporated available image stamps, colour composites, residual images, and the best-fit Sérsic indices. Additionally, unsharp-masked versions of the images were also shown to the classifiers to enhance fine details and highlight distinct features that might otherwise be overlooked. To facilitate the classification process, given the large sample size of approximately 10,000 images, we used a custom classification tool for galaxy morphologies (*GALCLASS*⁷).

Our visual classification categorizes the galaxies in the sample based on their morphological features, emphasizing structural characteristics such as compactness, diskiness, interaction signatures, and lensing distortion. Below, we outline the main categories used in the classification:

i) **Disk:** These galaxies are characterized by a distinct, organized structure with a Sérsic index close to unity, consistent with Wuyts et al. (2011b), who showed that $n \sim 1$ is typical for main sequence galaxies. They often show spiral arms and may have a central bulge. Depending on the viewing angle, they can appear circular, oval, or linear, corresponding to face-on, intermediate, or edge-on orientations.

ii) **Compact-Spheroidal:** These systems appear smooth and rounded, with no visible disk or spiral structure. They have a uniform brightness profile and are typically featureless. When

classifying these galaxies, we also considered their Sérsic indices, selecting systems that were well described by $n \approx 4$.

iii) **Interacting/Merger:** Interacting or merging galaxies exhibit irregular and distorted shapes due to gravitational interactions. Common features include tidal tails, bridges between galaxies, and unusual shapes, often indicating ongoing collisions or close proximity to another galaxy.

iv) **Undefined:** This category includes galaxies that lack any well-defined structure but do not show clear interaction features. They appear disordered, fragmented, or amorphous, without the characteristics of disks, spheroids, or mergers.

Within each category, we also included an option to identify the presence of companion galaxies as well as a strongly lensed system, identified by the presence of arcs, or rings of a background object gravitationally lensed by the foreground galaxy. For galaxies classified as disks, we also noted the presence or not of five non-exclusive morphological features labelled “Spiral”, “Bar”, “Bulge”, “Clumpy”, and “Edge-on”, several of which may be present in a given galaxy. Figure 4 provides an overview of the classification scheme, showcasing the main categories and representative examples of each category and subcategory with colour composite images. These images were generated using *TRILEGY* (Coe et al. 2012), with filter groupings carefully selected to enhance the visibility of key galaxy features. Specifically, shorter-wavelength filters were assigned to blue, longer-wavelength filters to red, and intermediate-wavelength filters to green, ensuring a balanced colour representation. An equal number of filters (where possible) were distributed across the RGB channels to maintain consistency in the visualization.⁸

⁸ The individual images used to generate the colour composites were not PSF-matched. While variations in PSF size exist across filters, the impact on the colour images is generally minor, as the broad structural features of galaxies remain visually consistent. Moreover, these images

⁷ <https://github.com/spastras/galclass>

Table 2: Classification results based on our 4/6 expert vote threshold, showing the main morphological categories and their distribution across redshift bins. The top rows list total fractions normalized by the full sample, while the middle section details subcategories among disk galaxies. The bottom rows present the distribution of spiral arm counts.

Type	f definition	Total		$0.8 < z < 1.3$		$2.0 < z < 2.5$	
		N	$f(\%)$	N	$f(\%)$	N	$f(\%)$
Total	$N_{\text{total}}/N_{\text{total}}$	1,451	100	811	100	640	100
Disk-like	$N_{\text{disk}}/N_{\text{total}}$	1,186	82	727	90	459	72
Compact/Sph	$N_{\text{c,s}}/N_{\text{total}}$	24	2	17	2	7	1
Int/Merger	$N_{\text{i,m}}/N_{\text{total}}$	139	10	48	6	91	14
Undefined	$N_{\text{undefined}}/N_{\text{total}}$	22	2	11	1	11	2
+ Lens systems	$N_{\text{lens}}/N_{\text{total}}$	3	< 1	1	1	2	< 1
+ Companion	$N_{\text{+companion}}/N_{\text{total}}$	67	5	32	4	35	6
No 4/6 agreement	$N_{\text{no-agree}}/N_{\text{total}}$	80	6	8	1	72	11
Spirals	$N_{\text{spiral}}/N_{\text{total}}$	574	40	444	55	130	20
Bars	$N_{\text{bar}}/N_{\text{total}}$	43	3	42	5	1	< 1
Bulges	$N_{\text{bulge}}/N_{\text{total}}$	703	48	495	61	208	33
Spirals	$N_{\text{spiral}}/N_{\text{disk}}$	574	48	444	61	130	28
Bars	$N_{\text{bar}}/N_{\text{disk}}$	43	4	42	6	1	< 1
Bars (isophotal fitting)	$N_{\text{bar}}^{(a)}/N_{\text{disk}}^{(b)}$	84	11	74	16	10	3
Bulges	$N_{\text{bulge}}/N_{\text{disk}}$	703	59	495	68	208	45
Clumpy	$N_{\text{clumpy}}/N_{\text{disk}}$	140	12	81	11	59	13
Edge-on	$N_{\text{edge-on}}/N_{\text{disk}}$	167	14	113	16	54	12
Two-arm spirals	$N_{2,\text{arm}}/N_{\text{spiral}}^{(c)}$	208	61	156	60	52	64
Three-arm spirals	$N_{3,\text{arm}}/N_{\text{spiral}}^{(c)}$	104	30	79	30	25	31
Four-arm spirals	$N_{4,\text{arm}}/N_{\text{spiral}}^{(c)}$	18	5	15	6	3	4

Notes. ^(a) These values correspond to the classification using isophotal fitting on a larger candidate sample, selected with a 2/6 voting threshold and further assessed as detailed in §3.2.

^(b) These values correspond to those with an ellipticity threshold of $e < 0.5$.

^(c) N_{spiral} in the bottom rows corresponds to the number of galaxies for which a 4/6 agreement was reached (343 galaxies).

The final classification was determined based on a consensus threshold, requiring at least 4 out of 6 expert votes for a category assignment. We emphasize that galaxies failing to meet this threshold for any category remain unclassified, which is distinct from the “Undefined” category, as the latter represents galaxies with inherently disordered shapes or non-coherent structures, and is thus a category on its own.

3.2. Classification overview

Our visual classification results, based on the 4/6 voting threshold (Table 2 and Figure 6) reveal that the majority of galaxies in our sample have a disk-like morphology, comprising 82% of the total sample ($\approx 90\%$ and $\approx 72\%$ in the low- and high-redshift bins, respectively). Interacting/merging galaxies form the second-largest category, accounting for $\approx 10\%$ of the sample, with a notable increase in the higher redshift bin. Spheroidal galaxies make up only 1.7% of the sample, with slightly more found in the lower redshift bin. Lensed systems and undefined galaxies are rare, representing 0.1% and 1.5%, respectively. Notably, only 80 galaxies (5.5%) lacked a 4/6 voting agreement.

An important potential bias to consider in the classification of galaxies (whether through visual or automatic methods) is related to their apparent size. Specifically, we observe increasing disk fractions f_{disk} as a function of r_{eff} as shown in Figure 7, where we show f_{disk} in bins of $\Delta r = 0.1$ arcsec. This is expected since it is easier to identify a disk-like structure in ex-

tended sources. However, this trend may also have a physical origin, as disks typically exhibit extended light distributions, which naturally results in larger effective radii and contributes to the observed correlation.

A more extended discussion of observational limitations, such as resolution differences and surface brightness dimming effects, is provided in Appendix A.

3.3. Classification of substructures

3.3.1. Spiral structure

Despite the lack of consensus on the origin of spiral structure, its connection to the dynamical state of the host galaxy is well supported (see reviews by Dobbs & Baba 2014; Shu 2016; Sellwood & Masters 2022). Spiral structure arises in disks that are sufficiently cold and rotationally supported, offering an indirect tracer of a galaxy’s mass distribution and instability to non-axisymmetric perturbations (e.g., Athanassoula 1984; Toomre 1964; Sellwood & Carlberg 1984). Identifying spiral arms, therefore, indicates that the galaxy hosts a settled disk, responsive to internal or external perturbations (e.g., Dobbs & Baba 2014).

Beyond their presence alone, the number of spiral arms also encodes information about the underlying dynamics (e.g., Elmegreen & Elmegreen 2014; Dobbs & Baba 2014). While two-armed (grand-design) spirals are likely driven by global disk modes or external perturbations, such as bars or tidal interactions (e.g., Toomre & Toomre 1972; Athanassoula 1984; Dobbs et al. 2010; D’Onghia et al. 2013; Kendall et al. 2015), multi-armed (flocculent) spirals typically emerge in marginally sta-

are intended solely for visual representation of the sample, and no quantitative measurements are derived from them.

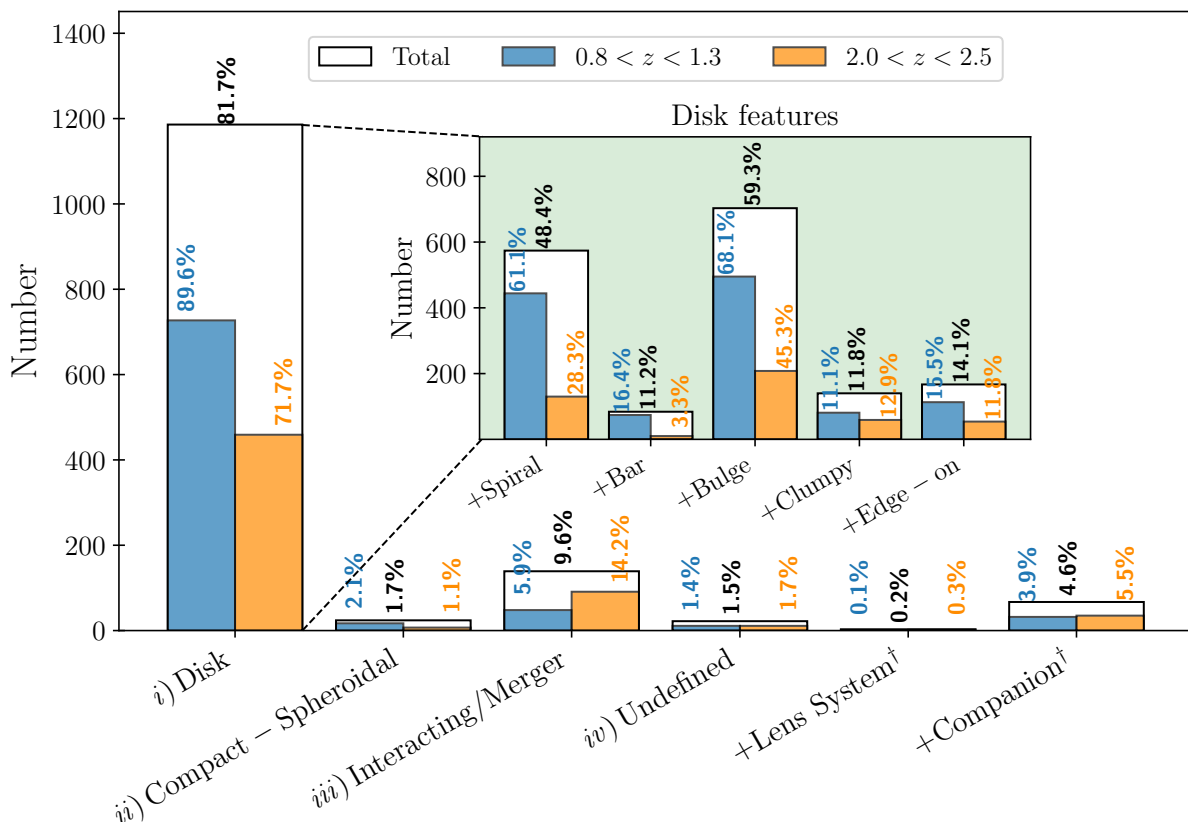


Fig. 6: Global classification results for the 1,451 galaxies in our sample. The blue and orange bars represent the low- and high-redshift bins, respectively, while the white bars correspond to the full sample. The percentages on top of the bars correspond to fractions normalized by the number of galaxies in the full sample, with black for the total, and blue and orange for the two redshift bins. The inset figure highlights the galaxies classified as disks in the sample, for which we also note the presence or not of five morphological features. The percentages displayed on top of those bars indicate the fractions of each subcategory normalized by the total number of disks. The † symbol in “+ Companion” denotes a non-mutually exclusive category, meaning it can be assigned alongside any of the main categories.

ble disks through mechanisms like swing amplification (Toomre 1981). As such, both the detection and characterization of spiral arms (particularly arm multiplicity) offer key diagnostics of disk structure, stability, and the mechanisms shaping galaxy evolution (e.g., Hart et al. 2017).

To investigate potential trends in spiral structure across our two redshift bins, we visually counted the number of arms within the spiral galaxies identified in our classification (574 in total). Following a similar approach used for morphological classification, six authors (J.M.E.S., C.B., C.P., J.C., J-B.J., G.T.) independently performed the arm counts. To aid in the identification of spiral arms, we utilized a custom interactive tool for visualizing FITS files with customizable scales using all the stamps for each galaxy. Each team member independently determined the number of visible arms for each galaxy. Figure 5 (bottom panels) shows examples of four galaxies with a consensus on the number of counted spiral arms. Figure 5 (bottom panels) provides examples of galaxies with consensus arm counts, while full-colour composite images of all classified spiral galaxies are available at this link. The results of the spiral arm counting are discussed in §4.

3.3.2. Bar structure

We identified barred galaxies in our sample by refining the initial visual classification through the fitting of elliptical isophotes. Since visually identifying bars can be challenging as they can be obscured by bright central bulges or may blend with spiral arms, we applied a more inclusive threshold of 2/6 classifier votes to ensure potential barred galaxies were not overlooked. The isophotal fitting method provides a quantitative test for confirming bar structures.

Starting from a parent sample of 123 galaxies that received at least 2/6 classifier votes for a bar, we applied an ellipse-fitting technique using `photutils` (Bradley et al. 2016) on images taken with the longest available wavelength filter (F444W, except for one case where F356W was used). We then analyzed the resulting ellipticity ($e = 1 - q$), where q is the axis ratio, as well as the position angle profiles as functions of radius to confirm the presence of bars. To classify a galaxy as barred, we imposed the following criteria: *i*) the galaxy must not be edge-on, defined as having an ellipticity below 0.5 at large radii, outside the regions influenced by the bar or spiral arms; *ii*) The ellipticity must increase smoothly with radius, reaching a well-defined peak above 0.25 before decreasing again, as expected for a bar. This ensures that the feature is significantly elongated and not an artifact of noise or a mild bulge elongation; and *iii*) the position

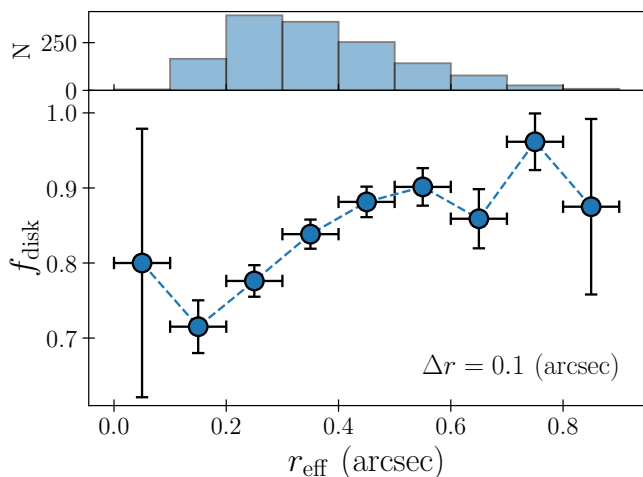


Fig. 7: Disk fraction as a function of effective radius (r_{eff}), measured in bins of $\Delta r = 0.1$ arcsec. The blue points represent the disk fraction in each bin, with error bars indicating binomial uncertainties. The dashed line connects the points for visualization. The fraction steadily increases with effective radius, which may reflect an intrinsic trend or the greater ease of visually identifying disks in larger galaxies. The histogram in the top panel shows the number of galaxies per bin, with lower counts in the first and last bins (5 and 8 galaxies, respectively), contributing to the larger uncertainties in those bins.

angle must remain relatively constant (within 20°). We show an example of this analysis in Figure 8, with the identification of a bar for galaxy GN4_10280.

With these additional criteria, the number of identified barred systems increased to 84, with 74 in the low-redshift bin and 10 in the high-redshift bin. Notably, 81 out of the 84 barred galaxies were also classified as spiral galaxies. Figure 5 (top panels) presents four examples of barred galaxies in our sample. The full mosaic of the colour images of the barred systems is available at this link⁹.

4. Morphological evolution

In this section, we present and interpret the results of our visual classification of morphologies, with a discussion on the various found trends across redshift.

4.1. Disks

Figure 9 compares the disk fractions $f_{\text{disk}} = N_{\text{disk}}/N_{\text{total}}$ derived from our study, with the kinematic analysis of KMOS^{3D} (Wisnioski et al. 2015) and a morphological classification by Ferreira et al. (2023). We find that our large disk fractions (90% and 72% in the low- and high-redshift bins, respectively) are consistent with the disk fractions estimated from the kinematic analysis of (Wisnioski et al. 2015) across the same redshift range. Additionally, our low-redshift results are also consistent with the findings of Tiley et al. (2021) (KGES) for their sample of 288 galaxies at $1.2 < z < 1.8$, where the $z \approx 0.9$ measurement comes from KROSS (Harrison et al. 2017) with $v/\sigma > 1$.

⁹ https://www.mpe.mpg.de/resources/IR/JWSTColorImages/barred_grid_A4.pdf

However, discrepancies arise when comparing our results to the visual classification results of Ferreira et al. (2023), even after applying similar stellar mass and star formation rate (SFR) cuts. These differences are likely driven by variations in classification schemes and sample selection criteria. In particular, Ferreira et al. studied a broader range of stellar masses, including low-mass systems within $\log(M_*/M_\odot) \approx [6.6, 11.5]$ in the range $1.5 < z < 6.5$ for *JWST* CEERS observations overlapping with the CANDELS EGS field. Our sample is much more massive with $\log(M_*/M_\odot) = [10, 11.4]$. When applying comparable mass cuts, the sample overlap is very limited: we identify only 44 galaxies in the similar low-redshift bin and 75 in the high-redshift bin, with 28 and 41 classified as disks, respectively.

Additionally, differences in classification criteria may contribute to the observed discrepancies. A key distinction in their approach is the “peculiar” category, which includes many galaxies that, in our classification, would likely be labelled as disks with a “clumpy” feature flag or “interacting/merger” or “undefined” when disk classification is uncertain. Another methodological difference lies in the choice of imaging filters: classified galaxies based on images taken in the filter that best matched the rest-frame optical wavelength at the source redshift (i.e., minimizing $\lambda_{\text{rest}}/(1+z)$), whereas we utilized imaging across all available filters.

4.2. Spirals

We use the results from the visual classification of spiral galaxies to assess the spiral fraction in the two redshift bins, as $f_{\text{spiral}} = N_{\text{spiral}}/N_{\text{total}}$. We find spiral fractions of 0.55 and 0.20 in the low- and high-redshift bins, respectively. It is worth noting that the remaining disks in our sample, which are not confidently classified as spirals, could still include galaxies with spiral features. These galaxies might not meet our criteria for confident identification due to factors such as near-edge-on orientations or small angular sizes. Consequently, the inferred spiral fractions could represent only a subset of the real population of disk galaxies with spiral features, as we prioritize robust classification over completeness.

As shown in Figure 10a, our inferred spiral fractions show general agreement with Kuhn et al. (2024), who also utilize *JWST* imaging. We compare both their uncorrected and corrected values, where the latter account for observational effects to estimate the intrinsic spiral fraction. While the overall trends are consistent, our results show a steeper decline in the spiral fraction with increasing redshift. As seen in Kuhn et al. (2024), applying corrections for these effects has a larger impact on the inferred intrinsic spiral fractions at higher redshifts. Both our results and those of Kuhn et al. find systematically higher spiral fractions compared to Margalef-Bentabol et al. (2022), whose measurements are based on *HST* imaging. This discrepancy is likely due to *JWST*’s superior sensitivity and improved spatial resolution in the near-IR, which enables the identification of more subtle spiral structures that might be missed in *HST* data. Additionally, *JWST*’s coverage of longer rest-frame wavelengths enhances the visibility of the underlying disk, boosting confidence in the identification of spirals.

This consistency supports the trend of a decreasing spiral fraction with increasing redshift, likely reflecting the progressive dynamical settling of disks over cosmic time. The presence of well-defined spirals at $z \approx 2$ suggests that some disks were already mature enough to sustain spiral structures, though they become increasingly rare at earlier epochs. However, this interpretation remains sensitive to observational limitations. As em-

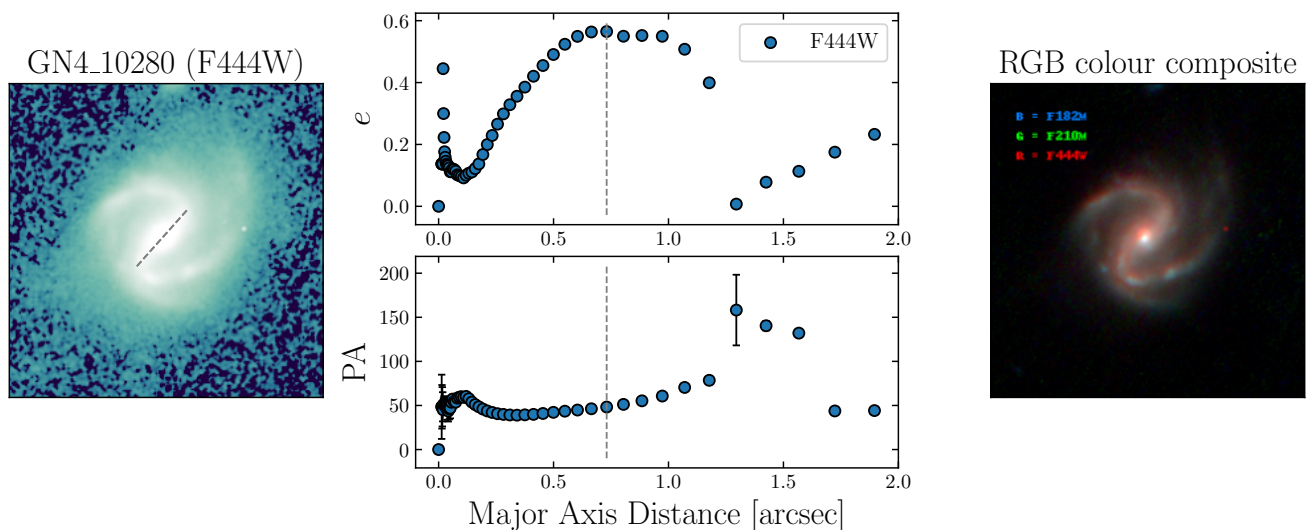


Fig. 8: Bar identification analysis for GN4_10280: Left: F444W image with the best-fit major axis of the bar indicated by the dashed line. Middle: Radial profiles of ellipticity (e , top) and position angle (PA, bottom) as a function of the major axis of the isophotes, extracted from the F444W image. The vertical dashed line marks the maximum in the ellipticity. Right: RGB colour composite using F182M (blue), F210M (green), and F444W (red), highlighting the galaxy’s structure in different wavelengths.

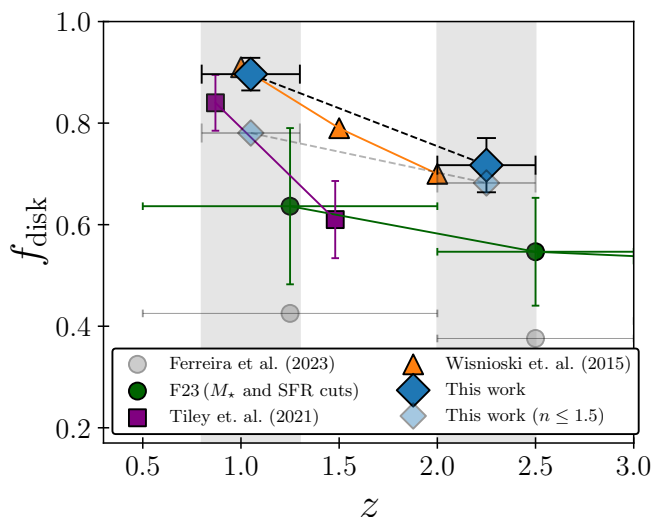


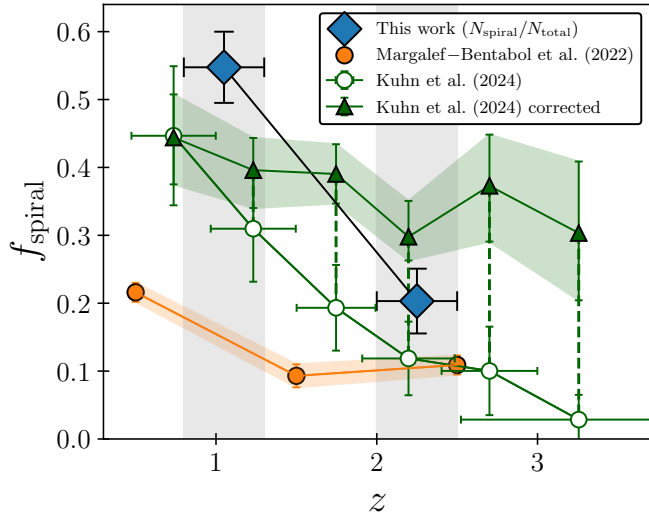
Fig. 9: Disk fractions, $f_{\text{disk}} = N_{\text{disk}}/N_{\text{total}}$, as a function of redshift. Blue diamonds represent results from our visual classifications, with 3σ standard errors estimated from a binomial distribution $\sigma = \sqrt{p(1-p)/N}$, with p the corresponding fraction and N the total number of galaxies in the parent sample. Light blue diamonds indicate disk fractions when an additional Sérsic index threshold of $n \leq 1.5$ is applied. For comparison, orange triangles indicate disk fractions from the kinematic analysis of Wisnioski et al. (2015), while purple squares show measurements from Tiley et al. (2021). Green circles represent disk fractions for the subset of the 3D-HST galaxies in (Ferreira et al. 2023) (F23) that overlap with our sample and satisfy our M_* & SFR selection criteria. Grey circles correspond to the unfiltered but still overlapping sample of F23. The gray-shaded regions indicate the redshift bins analyzed in this study.

phasized by Kuhn et al. (2024), the apparent decline is significantly reduced when accounting for these effects.

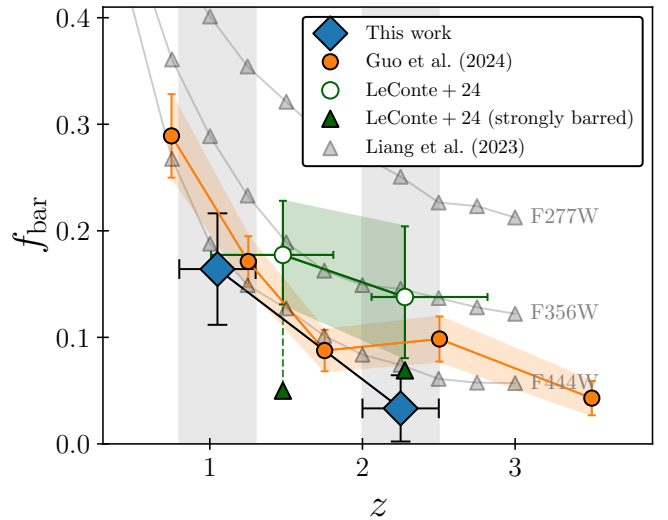
Beyond the overall fraction of spirals, their internal structure also shows striking consistency across redshifts. Applying the same 4/6 voting threshold as in the broad morphological classification, we determined the number of spiral arms in the subset of galaxies that met this criterion. Among the 574 classified galaxies, 343 surpassed this threshold, representing 59.4% of the sample. This includes 260 out of 444 galaxies in the low redshift bin (58.6%) and 81 out of 130 in the high redshift bin (62.3%). We show the number of galaxies as a function of their identified number of spiral arms in Figure 11, with percentages normalized by the number of spiral galaxies in each redshift bin, for which a consensus of 4/6 votes was reached. We find relatively close agreement between the two redshift bins in the normalized arm number fractions, with approximately two-thirds of galaxies exhibiting two arms and about one-third showing three arms in both bins. This suggests little evolution in spiral arm multiplicity across these cosmic epochs.

Interestingly, our visual classification of spiral arm multiplicity reveals trends broadly consistent with those observed in the local Universe. In both the $0.8 < z < 1.3$ and $2.0 < z < 2.5$ bins, two-armed spirals remain the dominant morphology, with a fraction comparable to that reported by Hart et al. (2016), who analyzed 62,220 SDSS galaxies from Galaxy Zoo in the redshift range $0.03 < z < 0.085$. For comparison, we use their luminosity-limited subsample ($M_r \leq -21$), which spans the same stellar mass range as our data ($\log(M_*/M_\odot) = [10, 11.5]$) and includes debiased fractions to correct for classification biases arising from redshift-dependent effects. Although we do not apply a formal debiasing correction, this adjusted low-redshift baseline provides a useful reference point for interpreting trends at higher redshift.

The agreement in two-arm dominance suggests that grand-design spiral patterns were already common by $z \sim 1-2$ and supports the idea that many high-redshift disks were already cold and massive enough to sustain global $m = 2$ modes, either spontaneously, aided by torques introduced by bars or through external drivers such as interactions (e.g., Toomre & Toomre 1972; Athanassoula 1984; D’Onghia et al. 2013; Dobbs & Baba 2014). Although the prevalence of two-armed spirals



(a) Spiral fractions defined as $f_{\text{spiral}} = N_{\text{spiral}}/N_{\text{total}}$ for comparison with other studies. Green dots and triangles represent the *JWST*-based results from (Kuhn et al. 2024), where the white circles show the directly measured spiral fractions, and the filled triangles indicate the values after applying corrections for observational effects. Orange dots represent the fractions inferred from *HST* imaging in the CANDELS fields by (Margalef-Bentabol et al. 2022).



(b) Bar fractions ($f_{\text{bar}} = N_{\text{bar}}/N_{\text{disk}}$) from the subsample of disks with $e < 0.5$ where the isophotal fitting analysis is reliable. Orange dots show the results from Guo et al. (2024), while green dots correspond to the fractions inferred by Le Conte et al. (2024), with green triangles indicating the fractions inferred using only their sample of strongly barred galaxies. Grey triangles represent simulated bar fractions from Liang et al. (2023) for a set of *JWST* filters, given an intrinsic f_{bar} of 68% at $z \approx 0$.

Fig. 10: Comparison of spiral (left) and bar (right) fractions as a function of redshift. Blue markers represent results from our visual classifications, with 3σ error bars, which, similarly to the disk fraction errors, are estimated from a binomial distribution $\sigma = \sqrt{p(1-p)/N}$, where p is the fraction and N is the total number of galaxies in the parent sample.

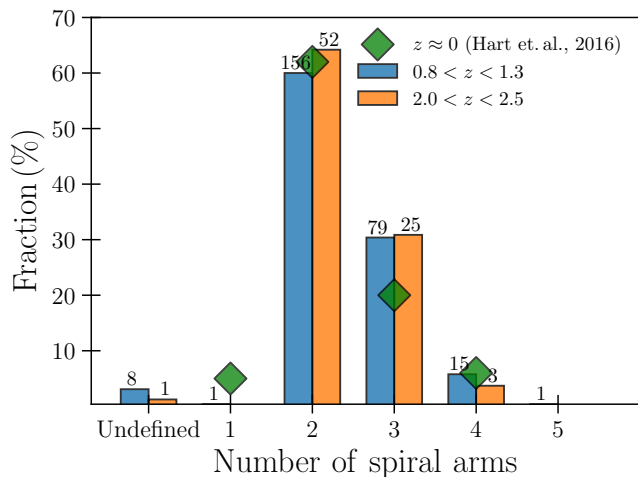


Fig. 11: Distribution of the number of spiral arms identified from visual classification, using a threshold of 4 out of 6 classifiers for agreement. The “Undefined” category refers to systems where classifiers agreed that no specific number of spiral arms could be discerned. The y-axis represents the fraction of spiral galaxies in each redshift bin, normalized by the total number of classified spiral galaxies in that bin. The blue bars correspond to galaxies in the $0.8 < z < 1.3$ range, while the orange bars represent galaxies in the $2.0 < z < 2.5$ range. Numbers displayed above the bars indicate the absolute counts of galaxies in each category. The green diamonds correspond to the debiased fractions from the luminosity-limited sample of Hart et al. (2016).

appears stable, their structural properties may still evolve. For instance, Chugunov et al. (2025) find that pitch angles tend to increase with redshift, suggesting that high-redshift spirals are more loosely wound than their low-redshift counterparts.

Beyond the dominant two-arm population, we find a noticeably higher incidence of three-armed spirals in our sample: while Hart et al. (2016) report that about 20% of local spirals have three arms, we find a higher fraction (30%), pointing to a modest increase in three-fold symmetry at earlier epochs. The relative excess of three-armed systems in our study could be the result of different disk properties at cosmic noon, such as higher gas fractions (e.g., Tacconi et al. 2020). Interestingly, recent simulations have identified the emergence of three-armed spirals in turbulent, gas-rich disks at high redshift, preceding the formation of a two-armed spiral or a bar (Bland-Hawthorn et al. 2024). Notably, one of the earliest high-redshift spirals observed with resolved structure also exhibits a three-armed morphology (Law et al. 2012). In agreement with these results, our results offer the first evidence for an increased incidence of the three-armed spiral morphologies at cosmic noon.

4.3. Bars

We estimated the bar fractions as $f_{\text{bar}} = N_{\text{bar}}/N_{\text{disk}}$, obtaining $\approx 16\%$ in the low-redshift bin and $\approx 3\%$ in the high-redshift bin. This overall decline with redshift is consistent with theoretical expectations that bars form more readily in dynamically cold, well-settled disks, which become increasingly common at lower redshifts. Supporting this, Sheth et al. (2008) found that bar fractions exceed 60% at $z \approx 0$, but are expected to decline

toward earlier epochs due to higher gas fractions and increased turbulence in young disks.

Our measured bar fractions, shown in Figure 10b, are broadly consistent with those reported in recent high-redshift *JWST* studies such as Guo et al. (2024) and Le Conte et al. (2024), though we report slightly lower values, particularly in the high-redshift bin. Guo et al. used NIRC*am* F200W and F444W data from CEERS, combining ellipse fitting and visual inspection to identify bars. Le Conte et al., using CEERS+PRIMER data in F444W, reported higher bar fractions by including both “strongly” and “weakly” barred systems. In their classification scheme, galaxies with at least 3/5 votes for barred were labelled strongly barred, while those with 2/5 votes for barred or at least 3/5 for maybe-barred were considered weakly barred. When considering only the strongly barred subset, their bar fractions drop to 5%–7% for the redshift range $1 < z < 3$, closely matching our measurements within uncertainties.

We also compare our results with Liang et al. (2023), who artificially redshifted nearby galaxies, applying realistic size and luminosity evolution, and simulated NIRC*am* observations at CEERS depth across multiple filters. Using a bar-size detection threshold of $a_{\text{bar}} > 2 \times$ the PSF FWHM, their recovered trend in bar fraction also shows a decline with redshift, consistent with our findings.

Despite the overall agreement with previous studies, observational limitations must be carefully considered when interpreting the decline in bar fractions. Surface brightness dimming can obscure low-contrast bars, especially in faint or diffuse galaxies. Lian & Luo (2024) showed that near face-on spirals with faint arms may be misclassified as edge-on systems, further complicating bar identification. In addition, spatial resolution constraints limit the detectability of small-scale bars, particularly at high redshift, where structural features approach the PSF scale and may remain unresolved. In our sample, for instance, bars smaller than 1.5–2 times the FWHM of the F444W PSF are not detected, consistent with the resolution threshold reported by Erwin (2018). These limitations suggest that the observed decline in bar fractions with redshift may reflect not only intrinsic evolution but also increasing challenges in detection at earlier epochs. The true bar fraction at high redshift may be higher than what is currently measurable.

This possibility becomes even more compelling in light of recent observations of rapid radial gas inflows in high-redshift star-forming barred galaxies (Genzel et al. 2023; Arriagada-Neira et al. 2024; Pastras et al. 2025, in prep) and even in dusty star-forming galaxies at $z > 3$ (e.g., Umehata et al. 2024; Amvrosiadis et al. 2025). If such inflows are common in early disk galaxies, they could play a crucial role in shaping the evolution of the host galaxies, modifying the conditions for bar instabilities (e.g., Bland-Hawthorn et al. 2024). Moreover, if baryons dominate the local gravitational potential over dark matter in these high-redshift galaxies (e.g., Genzel et al. 2017, 2020; Price et al. 2021; Nestor Shachar et al. 2023), stellar bars could form on rapid timescales of 1–2 Gyr, even in gas-rich turbulent disks (e.g., Fujii et al. 2018; Bland-Hawthorn et al. 2023, 2024), reinforcing the idea that bars at high redshift might be underestimated rather than intrinsically rare.

4.4. Interacting/Mergers

The fraction of galaxies classified as interacting or merging systems shows a clear decline with cosmic time, decreasing from 14.2% in the higher redshift bin ($2.0 < z < 2.5$) to 5.9% in the lower redshift bin ($0.8 < z < 1.3$). This trend aligns with the

expected decrease in merger activity at lower redshifts, driven by declining galaxy densities and interaction rates (e.g., Conselice 2007; Lin et al. 2008; Lotz et al. 2008; Rodriguez-Gomez et al. 2015). Despite our modest sample size, this decline remains consistent with theoretical and observational predictions in the framework of the hierarchical growth model in which major mergers become less frequent at later cosmic times.

5. Quantitative morphological metrics

We performed a quantitative analysis of the morphological properties of the sample to complement the visual classification. To achieve this, we employed several established non-parametric morphological indicators commonly utilized in morphological studies to characterize the structural features of the galaxies in our sample. These metrics include the Concentration, Asymmetry, and Smoothness (CAS) statistics (Conselice 2003), the Multinode, Intensity, and Deviation (MID) statistics (Freeman et al. 2013), and the Gini and M_{20} coefficients (Lotz et al. 2004). All measurements are quantified using *STATMORPH* (Rodriguez-Gomez et al. 2019). Here is a brief description of them.

CAS: Concentration (C) quantifies the distribution of light within a galaxy, typically by comparing the radii containing 80% and 20% of its light, characterizing the galaxy’s core. Asymmetry (A) evaluates the symmetry of the light distribution by comparing the original image with a version rotated by 180 degrees, often used to identify mergers or irregularities. Smoothness (S), also referred to as clumpiness, measures the fraction of light associated with small-scale structures, distinguishing smoother elliptical galaxies from clumpier, irregular galaxies or prominent spiral arms.

MID: The Multinode, Intensity and Deviation (MID) statistics allow for the identification of disturbed morphologies, such as mergers or interacting systems. Multinode (M) measures the presence of multiple peaks in the light distribution, indicating complex or multi-component structures. Intensity (I) assesses the brightness contrast between these peaks and their surroundings, highlighting areas of intense star formation or disruptions. Deviation (D) quantifies the departure of the light distribution from a smooth, symmetric model, further aiding in the detection of structural disturbances.

Gini and M_{20} coefficients: The Gini (G) coefficient characterizes the distribution of the flux among the pixels assigned to an extended source. It varies from 0 to 1, where $G = 0$ corresponds to a uniform distribution (all pixels contain the same flux), and $G = 1$ corresponds to the flux being concentrated in a single pixel. The M_{20} coefficient, which quantifies the second-order moment of the brightest 20% of the galaxy’s flux relative to the total light distribution, helps in identifying the spatial extent and configuration of bright regions, so it is a useful metric to quantify the degree of morphological disturbance.

We ensured consistency across the sample at different redshifts by applying PSF matching, selecting uniform rest-frame wavelengths, and masking with segmentation maps. The rest-frame wavelength for morphology analysis was set to $\lambda_{\text{RF}} = 1.37 \mu\text{m}$, chosen as it corresponds to the optimal wavelength where the majority of galaxies in both redshift bins in our sample (1,300 out of 1,451) have imaging, F277W for the low-redshift bin and F444W for the high-redshift bin, both of which are wide filters, ensuring high signal-to-noise ratios. Spatial resolution differences were minimized by matching the PSF to a target resolution corresponding to the largest physical PSF in the sample (1.19 kpc). The detailed methodology, including wavelength and

PSF matching, segmentation map creation, and masking procedures, is described in Appendix B.

To assess the robustness of the morphological indicators, we conducted a systematic visual inspection of diagnostic images produced by *STARMORPH* (e.g., Figure 4 in Rodríguez-Gomez et al. 2019). The reliability of each measurement was assessed based on the following criteria: How well the model replicates the galaxy’s light distribution (e.g., the agreement between the observed and model images); quality of the residual image, where well-fit galaxies exhibit minimally structured residuals and poor fits show significant leftover flux or systematic artefacts; convergence of fitted parameters, ensuring they fall within physically reasonable ranges; and absence of contamination from neighbouring sources or image artefacts that could bias measurements. The evaluation of these diagnostic images, along with assessments of segmentation maps and PSF matching, were used to ensure the accuracy of the non-parametric morphological measurements. After applying this filtering process, we identified a high-quality subset of 1,222 galaxies that met our reliability criteria. We adopt this subset for the results and analysis presented in this work.

5.1. Dependence on redshift and stellar mass

In the majority of the derived morphological indicators, including concentration (C), Gini, Asymmetry, and M_{20} , we observe little to no evolution with redshift but notable trends with galaxy mass. Specifically, more massive galaxies tend to exhibit higher concentrations and Gini values, indicative of more compact and centrally concentrated light distributions, while M_{20} , indicative of morphological disturbance, shows a clear decreasing trend with increasing galaxy mass. The lack of significant redshift evolution suggests that the overall structural properties of galaxies, as captured by these metrics, remain relatively stable for ~ 2.7 Gyr between the median redshifts of 1.05 and 2.25 probed in our sample, and are primarily dependent on the stellar mass. These findings are consistent with trends previously identified in *HST* studies (e.g., Wuyts et al. 2011b; Lang et al. 2014).

Our findings also agree with trends reported in the literature, particularly in Yao et al. (2023) and Ren et al. (2024), which similarly noted stable morphological indicators across redshifts but a clear dependence on galaxy stellar mass. Figure 12 illustrates these comparisons, showing the mean values reported by Yao et al. (2023) for a F444W-matched sample in the redshift range $0.8 < z < 3$, as well as the median values from Ren et al. (2024) for $0.5 < z < 3$. To enable a consistent comparison, we reverse-applied the observational corrections used in Ren et al. (2024) to their data, which accounted for effects such as noise and finite PSF resolution, aligning their values with our F444W-matched dataset. In both cases, we find a strong agreement between the trends in our analysis and those reported by these studies.

5.2. Connection with visual classification

With the extensive set of morphological parameters computed in this analysis, we systematically explore how different galaxy classifications separate across various parameter spaces derived from *STARMORPH*. Specifically, we identify parameter combinations that effectively distinguish galaxies with and without bulges, mergers and non-mergers, and clumpy versus non-clumpy galaxies. To quantitatively assess the separation between classifications, we compute a *separation efficiency* metric based on misclassification rates. The methodology for defining and cal-

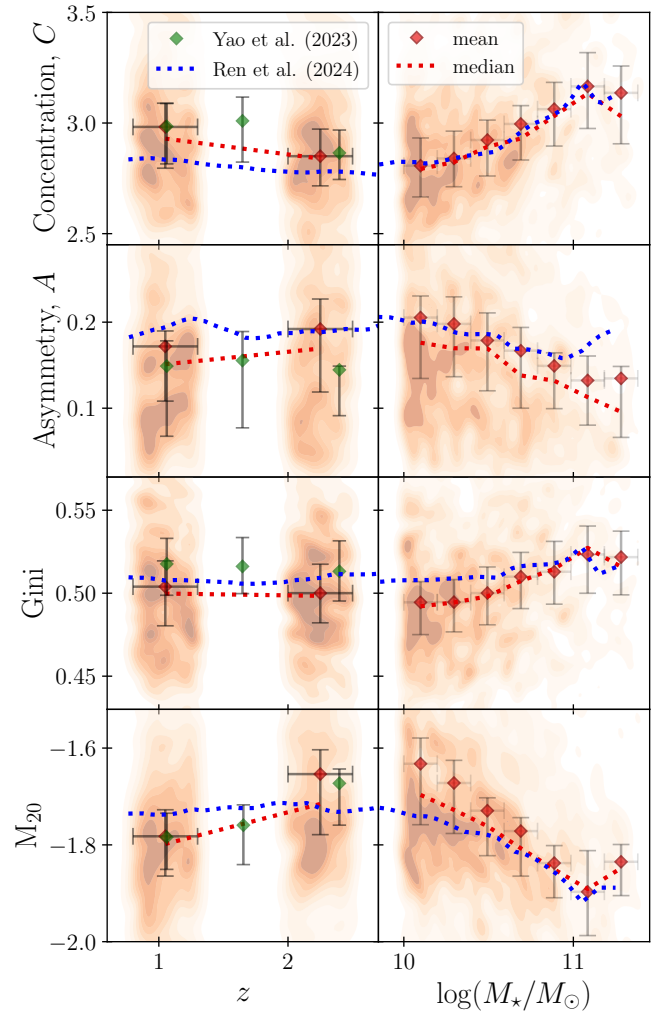


Fig. 12: Morphological statistics of galaxies across redshift (left column) and stellar mass (right column). From top to bottom: Concentration (C), Asymmetry (A), Gini, and M_{20} indices. Our results are presented as mean values (diamonds) and medians (horizontal markers). For comparison, we include the trends reported by Yao et al. (2023) (green diamonds) over the range $0.8 < z < 3$ and Ren et al. (2024) (blue dotted lines) for $0.5 < z < 3$. Our error bars indicate the central 34% range (spanning the 33rd to 67th percentiles) to ensure consistency with the results of Yao et al. The values from Ren et al. were originally adjusted for observational effects, such as noise and finite PSF resolution, using a correction formula. To ensure a consistent comparison with our F444W-matched galaxy sample, we reverse-applied their correction formula to de-adjust their values, aligning them with the observational conditions in our work and those by Yao et al. We find a strong agreement between our results and those of Yao et al. (2023) and Ren et al. (2024), highlighting the consistency across studies.

culating this metric, including the optimization of classification boundaries, is detailed in Appendix C, where we provide a full set of separation efficiencies for each classification. Given the wealth of possible parameter combinations, we highlight only the most informative and physically meaningful ones, prioritizing those that offer the clearest distinctions between morphologi-

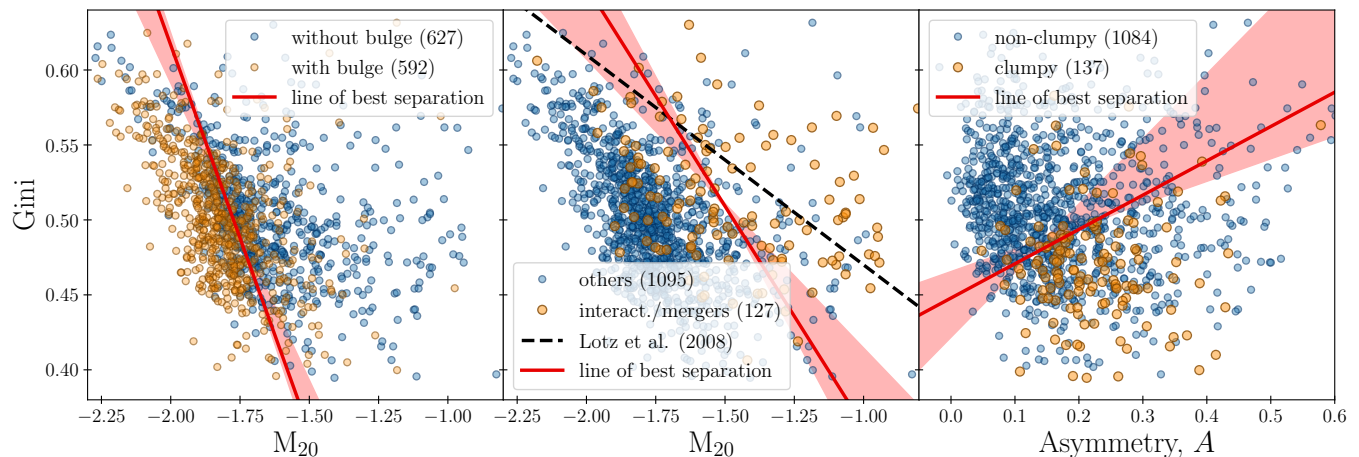


Fig. 13: Notable parameter spaces where the combination of morphological metrics separate well different morphologies. In each panel, the red line corresponds to the line of best separation, which corresponds to the minimal contamination C_{\min} (defined in Appendix C), and the light red area indicates other possible line positions which achieve contamination within 0.01 of the minimal contamination, i.e., $C \in (C_{\min}, C_{\min} + 0.01)$. *Left*: Gini vs M_{20} plane for galaxies with and without bulges. The line $G = -0.52M_{20} - 0.4$, separates the main cluster of galaxies with bulges (71%) and those without bulges (74%). *Middle*: Gini vs M_{20} plane for galaxies identified as interacting/mergers. The line $G = -0.29M_{20} + 0.07$ (red) shows a systematic separation of the cluster of datapoints in this parameter space, with 50% of visually classified mergers and 93% of non-mergers correctly separated. For comparison, we show with the black dashed line the boundary line established by Lotz et al. (2008) and discuss the difference in the main text. *Right*: Gini vs Asymmetry A plane for clumpy and non-clumpy galaxies. The separation line is given by $G = 0.229A + 0.448$, with 81.8% of clumpy galaxies below it and 64.1% of the non-clumpy galaxies above.

cal classes that have also been studied in the literature. However, all possible combinations, including those not well studied in other studies are presented in Tables C.2-C.4.

We emphasize that, with *JWST*'s unprecedented resolution, wavelength coverage, and depth, widely used morphological metrics, originally designed for lower-resolution datasets such as *HST* imaging, must be carefully reassessed. However, in this study, we focus on identifying broad, top-level trends in our sample rather than proposing precise recalibrations of these classification boundaries. A robust recalibration, which is beyond the scope of this work, should be carried out using larger statistical samples that fully leverage the growing wealth of high-quality *JWST* data, as well as the extensive galaxy catalogues from ongoing large surveys produced with EUCLID, which will provide millions of galaxies at local and intermediate redshifts (e.g., Euclid Collaboration et al. 2025a,b).

Bulges: For galaxies visually identified as containing bulges, the Gini- M_{20} plane provides one of the strongest separations between bulge-dominated and non-bulge galaxies (left panel of Figure 13). The optimal separation line, given by $G = -0.52M_{20} - 0.41$, correctly separates 74% of galaxies without bulges, as shown by the clear systematic offset between the two populations in the figure. This offset aligns with previous studies (e.g., Conselice 2003; Lotz et al. 2008), which demonstrated that non-parametric morphology indicators are effective in distinguishing bulge-dominated galaxies. The correlation between bulge presence, high Gini values, and low M_{20} values supports the interpretation that bulge-dominated galaxies have centrally concentrated light distributions and less fragmented substructures, making them easier to identify in this parameter space. Specifically, low M_{20} values indicate that a galaxy's brightest pixels are concentrated near the centre, which is characteristic of systems with prominent bulges.

Beyond the Gini- M_{20} plane, M_{20} alone also serves as a strong discriminator. Additionally, combining M_{20} with either the Sérsic index or the effective radius further improves classification accuracy. A full summary of bulge separation efficiency is presented in Table C.2 in the Appendix.

Mergers: Several parameter combinations effectively distinguish interacting and merging galaxies, including the Gini- M_{20} plane, MID statistics, and CAS parameters. The full separation efficiencies for mergers and non-mergers are presented in Table C.3 in the Appendix.

In the Gini- M_{20} plane, we define a separation line that maintains a merger fraction of $\approx 10\%$, matching both our measured fraction and the findings of Lotz et al. (2008). The resulting threshold, given by $G = -0.29M_{20} + 0.07$, correctly captures 93% of non-mergers (middle panel of Figure 13). For comparison, we show the boundary line estimated by a dedicated study of mergers and morphology Lotz et al. (2008), which analyzed $\approx 3,000$ galaxies with *HST* imaging at $0.2 < z < 1.2$ and found a separation boundary of $G = -0.14M_{20} + 0.33$. We find notable differences between our classification and theirs, particularly a 0.15 slope difference in the separation line. Moreover, our separation achieves a contamination value of 0.57, while adopting the Lotz et al. boundary in our dataset would result in a higher contamination value of 0.74. The differences in our boundary lines likely stem from differences in sample selection, imaging depth, rest-frame wavelength, spatial resolution and classification objectives. Whereas Lotz et al. optimized their boundary specifically for merger detection, we focused on a wider range of morphologies. Despite these differences, the overall separation trends remain similar, reinforcing that Gini vs M_{20} remains a useful discriminator and is effective, at least in a global sense, within our sample.

Among the CAS statistics, the asymmetry parameter provides another useful merger discriminator. Figure 14 (top panel)

illustrates the separation, where visually identified mergers are skewed toward higher asymmetry values, while non-mergers peak at lower asymmetries. The separation threshold that maintains a merger fraction of 10% closely aligns with the empirical merger criterion proposed by Conselice (2003) (dashed black), reinforcing the utility of asymmetry as a merger diagnostic.

Similarly, the MID statistics also effectively separate mergers from non-mergers. As shown in the bottom panels of Figure 14, the Multinode (M), Intensity (I), and Deviation (D) distributions exhibit systematic differences between the two populations. Interacting systems consistently show higher values across all three statistics, reinforcing the idea that MID metrics capture morphological disturbances and asymmetries associated with mergers and their irregular light distributions.

Clumps: The Gini coefficient is particularly effective in distinguishing clumpy from non-clumpy galaxies, especially when combined with other morphological metrics. Among these, the Gini- A (asymmetry) plane provides the clearest separation (right panel of Figure 13), highlighting the strong correlation between light concentration and structural irregularity in clumpy systems. The complete set of separation efficiencies for clumpy galaxies is provided in Table C.4 in the Appendix.

6. Morpho-Kinematic Correlations

For this discussion, we focus on global morpho-kinematic trends on a population-wide angle rather than detailed substructures, examining how the identified morphologies relate with dominant dynamical support as measured by v/σ . We use the homogenized $v_{\text{rot}}(r_{\text{eff}})$ and σ_0 values obtained from various subsamples outlined in §2.3. Our analysis reveals a notable distinction in the dynamical properties of galaxies classified as disks versus non-disks. For the 155 galaxies with kinematics measurements, 125 ($\approx 81\%$) were visually classified as disks, while 30 ($\approx 19\%$) were not identified as disks.

The histogram on the right of Figure 15 presents the v/σ distributions for visually classified disks and non-disks, where we examined their v/σ ratios relative to thresholds of 1, 3 and 10, commonly used in literature, corresponding to varying degrees of rotational support (e.g. Genzel et al. 2006; Kassin et al. 2012; Wisnioski et al. 2015; Wisnioski et al. 2019; Stott et al. 2016; Tiley et al. 2019; Gillman et al. 2020; Förster Schreiber & Wuyts 2020). A high v/σ ratio suggests a dynamically cold, rotation-dominated system typical of disk galaxies, whereas a low v/σ ratio indicates a dynamically hot, dispersion-dominated system signalling, e.g., more spheroidal geometries or stronger gravitational perturbations in merging systems.

Among the 125 visually classified disk galaxies, 88 (70%) have $v/\sigma > 3$, indicating strong rotational support. The remaining 37 disk galaxies (30%) have $v/\sigma < 3$, suggesting either weaker rotational support or the presence of non-circular motions (pure turbulence but also radial motions contributing to higher σ_0 in modelling of the typically seeing-limited IFU data included here). For non-disk galaxies, the trend is reversed. Only 12 galaxies (40%) have $v/\sigma > 3$, while the majority, 18 galaxies (60%), have $v/\sigma < 3$. This distribution reflects the expectation that non-disk galaxies exhibit lower rotational support, with their dynamics often dominated by random motions rather than ordered rotation. In the case of marginal rotational support of $v/\sigma = 1$, only 3 galaxies identified as disks and 5 from the other categories are below this boundary.

The apparent correlation between disk morphology and high v/σ is reassuring, yet it is important to consider observational limitations in the kinematics measurements that could affect the

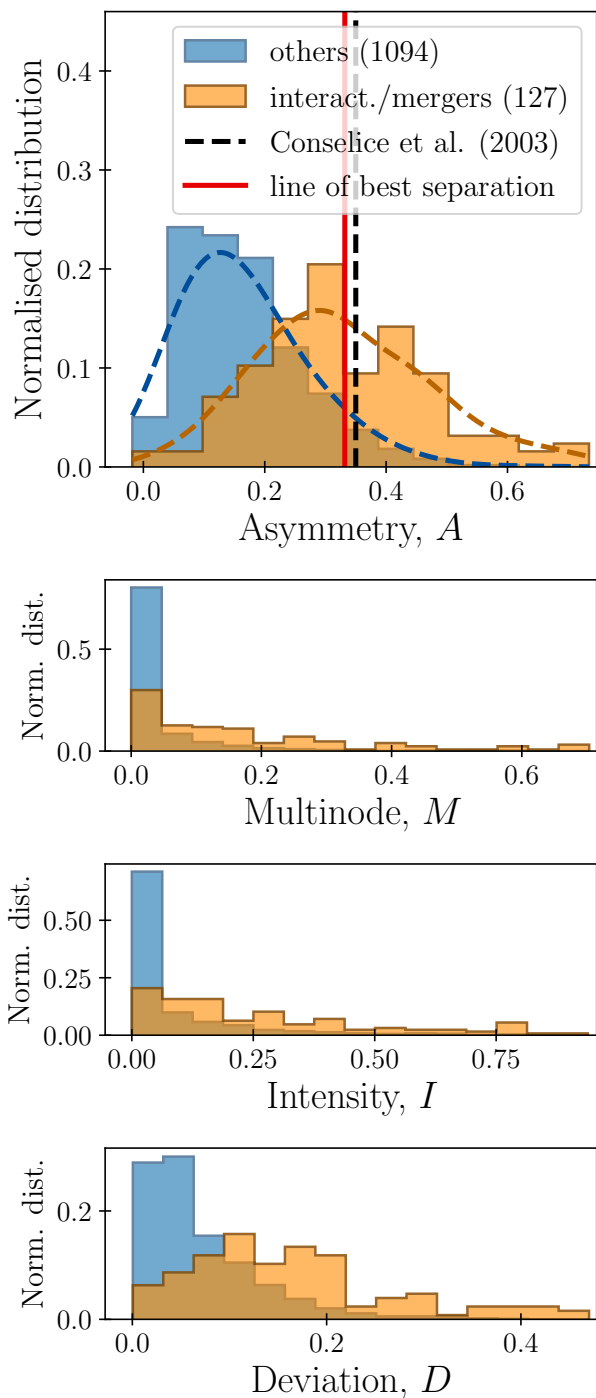


Fig. 14: *Top panel:* Distribution of the Asymmetry statistics (A in CAS) in our sample, which shows a clear systematic separation around value $A = 0.23$. Maintaining a merger fraction of $\approx 10\%$, we obtain the vertical red line $A = 0.332$ that separates 44% of mergers and 93% of non-mergers, with only a minor offset from the boundary line of $A = 0.35$ introduced by Conselice (2003). *Bottom three panels:* The Multinode, Intensity and Deviation (MID) statistics reveal systematic differences in distributions between visually classified mergers and non-mergers, as expected, given their design to capture morphological features of disturbed systems.

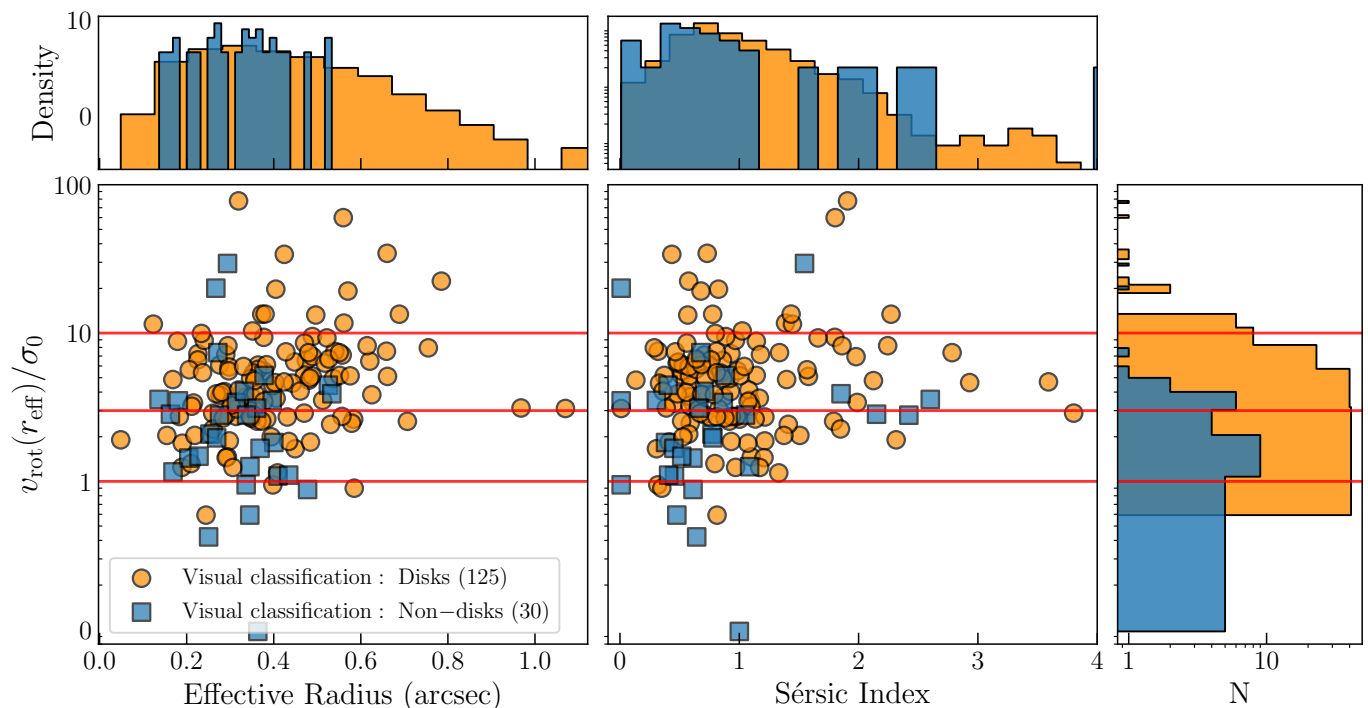


Fig. 15: Scatter plots of $v_{\text{rot}}(r_{\text{eff}})/\sigma_0$ as a function of effective radius (left) and Sérsic index (right) for disk (orange circles) and non-disk (blue squares) galaxies. The histograms above each panel show the normalized distributions of effective radius and Sérsic index, while the histogram on the right represents the distribution of $v_{\text{rot}}(r_{\text{eff}})/\sigma_0$. The red horizontal lines indicate reference values at $v_{\text{rot}}(r_{\text{eff}})/\sigma_0 = 1, 3, \text{ and } 10$.

correlation. One such effect is beam smearing, which artificially enhances velocity dispersions in smaller galaxies (e.g., Newman et al. 2013). In particular, compact galaxies at high redshift may exhibit inflated velocity dispersions due to unresolved velocity gradients, leading to an underestimation of their rotational support. Other key observational limitations include spectral resolution and the signal-to-noise ratio (S/N) of the emission lines (e.g., Davies et al. 2011). At high S/N, velocity dispersions can be reliably measured down to one-third of the spectral resolution, but at low S/N, noise-driven line broadening inflates dispersion estimates, biasing v/σ to lower values (e.g., Wisnioski et al. 2015; Übler et al. 2019).

Given the impact of beam smearing and S/N limitations, the observed correlation between disk morphology and high v/σ might be even stronger than what we found, with some dynamically cold disks being misclassified due to observational effects.

We further investigated how effective radius and Sérsic index correlate with measured v/σ ratios. To do this, we use the best-fit Sérsic parameters derived with `STATMORPH` on the sample that was matched in spatial resolution and rest-frame wavelength, as discussed in §5. The scatter plots in Figure 15 show v/σ ratios as a function of r_{eff} and n . In terms of the Sérsic indices, we find no discernible trend since there is a clear clustering of both disks and non-disks below a threshold of $n = 1.5$. In terms of the galaxy size, we detect a weak yet statistically significant positive correlation for disks between v/σ and the effective radius, with a Spearman correlation coefficient ($\rho = 0.26$, $p = 0.004$). While the correlation is weak, it aligns with theoretical expectations and the broader connection between galaxy size and dynamical structure observed in both simulations and observational studies (e.g., Dekel et al. 2013; Fall & Romanowsky 2013; Obreschkow & Glazebrook 2014; Teklu et al. 2015; Posti

et al. 2018; El-Badry et al. 2018; Tiley et al. 2021; Espejo Salcedo et al. 2025). Furthermore, larger disks are easier to visually identify in our classifications, making their structural properties more straightforward to analyze, as discussed in §3.2 and shown in Figure 7.

Beyond the technical aspects of classification agreement, these results provide insight into the nature of galaxy evolution at these redshifts. The strong connection between disk morphology and high v/σ suggests that a significant fraction of star-forming galaxies at cosmic noon are already dynamically settled and rotation-dominated. This is consistent with findings that a large fraction of galaxies at $z \sim 1 - 3$ exhibit regular rotation (e.g., Wisnioski et al. 2015; Johnson et al. 2018; Genzel et al. 2020; Tiley et al. 2021; Nestor Shachar et al. 2023). Moreover, we also find that a substantial fraction of these rotationally supported systems exhibit non-axisymmetric structures. Of the kinematically analyzed disks, 80 (64%) are classified as spirals, and 12 (10%) are classified as barred, with spiral structure, also identified in 10 of these. The median v/σ values further support the idea that these structures form in dynamically cold disks, with spirals showing a median $v/\sigma \approx 7$ and bars a slightly lower median of $v/\sigma \approx 5$. The slightly lower rotational support in barred galaxies may reflect additional kinematic complexities introduced by bars, such as radial motions that enhance velocity dispersions.

7. Conclusions

In this study, we analyzed a selected sample of *JWST* NIR-Cam images to investigate the morphological properties of 1,451 massive star-forming galaxies ($\log(\text{SFR}/\text{SFR}_{\text{MS}}) = [-0.4, 0.4]$) within a mass range of $\log(M_{\star}/M_{\odot}) = [10.0, 11.4]$, and sizes

within r_{eff} (arcsec) = [0.2, 1.0] at two key epochs within cosmic $0.8 < z < 1.3$ and $2.0 < z < 2.5$. We performed a global visual classification and identified key substructures such as bars and spirals. We complemented this with a quantitative analysis of morphology as a function of redshift and stellar mass and investigated links between morphology and kinematic properties where available. Our main findings are the following:

- *Global morphologies*: Based on our visual classifications, we find that the majority (82%) of our massive main-sequence galaxies exhibit disk morphology, while the rest are Spheroidal (1.7%), Interacting/Mergers (9.6%), and Undefined (1.5%). We also identify 0.2% of the sample as Lensed Systems and 5% as having companions. The rest of the sample did not reach the 4/6 voting threshold of our classification scheme.
- *Spirals*: At least 48% of visually identified disks feature spiral structures. A follow-up classification counted the number of spiral arms. We found similar distributions across the two redshift bins in this study across the sample: roughly two-thirds of spirals have two arms (60–64%), and one-third have three arms (30–31%), while four-armed spirals are rare (4–6%). These fractions are based on galaxies that reached the 4-out-of-6 vote agreement threshold. While the fraction of two-armed spirals is consistent with $z = 0$ studies, we report for the first time an increased incidence of three-armed spirals at cosmic noon.
- *Bars*: We identify 84 barred systems with isophotal fitting, with 74 in the low-redshift bin and 10 in the high-redshift bin, corresponding to bar fractions among the disk galaxies of 16% and 3%, respectively. These values align with previous studies on bar identification. While the decline in bar fraction with redshift may reflect intrinsic evolution, it is also influenced by observational challenges, such as surface brightness dimming, resolution limitations, and the expected evolution of galaxy and bar sizes. Overcoming these limitations requires greater sensitivity to surface brightness and improved spatial resolution, particularly in the infrared—capabilities that future observatories such as the ELT will provide.
- *Quantitative morphological metrics*: Non-parametric indicators indicate no significant evolution with redshift but a strong dependence on mass. Exploring all possible parameter combinations, we identify optimal metrics for distinguishing specific morphological features, consistent with previous studies:
 - Bulges are best separated by Gini- M_{20} and by M_{20} alone.
 - Mergers are well distinguished using Gini- M_{20} , MID statistics, and CAS parameters.
 - Clumps are best identified with the Gini coefficient alone and the combination of Gini-Asymmetry.
- *Kinematics*: We find a strong correlation between disk morphology and high rotational support ($v/\sigma > 3$), with 70% of kinematically analyzed disks meeting this criterion. Disks with high v/σ also tend to have Sérsic indices near unity and correlate modestly with r_{eff} , reinforcing the reliability of morphology-based classifications. A significant fraction of these rotationally supported galaxies exhibit non-axisymmetric structures: 64% are spirals, and 10% are barred, with all these barred systems being also spirals. These systems show large v/σ values, with spirals at a median $v/\sigma \approx 7$ and bars at $v/\sigma \approx 5$. While this difference is modest, the slightly lower v/σ in barred galaxies may reflect additional kinematic effects, such as radial motions increasing velocity dispersions.

Building on the findings presented here, we plan several follow-up studies. These include an investigation of the barred subsample and their kinematics to understand bar structures at high redshift better (Pulsoni et al., in prep), and an analysis of the connection between rapid inflows and non-axisymmetric substructures in gas-rich systems (Pastras et al., in prep). We also intend to examine metallicity gradients in disk galaxies to assess the role of radial mixing driven by bars and spiral arms.

Acknowledgements. We thank W. Maciejewski, A. Marchuk, S. Arriagada-Neira, and A. Burkert, for their valuable discussions and suggestions during the development of this work. J.M.E.S., N.M.F.S., G.T., C.B., and J.C. acknowledge financial support from the European Research Council (ERC) Advanced Grant under the European Union’s Horizon Europe research and innovation programme (grant agreement AdG GALPHYS, No. 101055023). HÜ acknowledges funding by the European Union (ERC APEX, 101164796). Views and opinions expressed are however those of the authors only and do not necessarily reflect those of the European Union or the European Research Council Executive Agency. Neither the European Union nor the granting authority can be held responsible for them. This work is based on observations made with the NASA/ESA/CSA *JWST* and complementary *HST* data obtained from the Mikulski Archive for Space Telescopes (MAST) at the Space Telescope Science Institute (STScI). We acknowledge the DAWN *JWST* Archive at the Cosmic Dawn Centre funded by the Danish National Research Foundation. We further appreciate the open-source software packages used throughout this work, including *ASTROPY* (Astropy Collaboration et al. 2013), *SCIPY* (Virtanen et al. 2019), *NUMPY* (van der Walt et al. 2011), *CMASHER* (van der Velden 2020), *MATPLOTLIB* (Hunter 2007), *GALFIT* (Peng et al. 2002, 2010), *STATMORPH* (Rodríguez-Gomez et al. 2019), *TRILOGY* (Coe et al. 2012).

References

- Abraham, R. G., Tanvir, N. R., Santiago, B. X., et al. 1996, *MNRAS*, 279, L47
 Amvrosiadis, A., Lange, S., Nightingale, J. W., et al. 2025, *MNRAS*, 537, 1163
 Arriagada-Neira, S., Herrera-Camus, R., Villanueva, V., et al. 2024, arXiv e-prints, arXiv:2410.14781
 Astropy Collaboration, Robitaille, T. P., Tollerud, E. J., et al. 2013, *A&A*, 558, A33
 Athanassoula, E. 1984, *Phys. Rep.*, 114, 319
 Bagley, M. B., Finkelstein, S. L., Koekemoer, A. M., et al. 2023, *ApJ*, 946, L12
 Bertin, E. & Arnouts, S. 1996, *A&AS*, 117, 393
 Bland-Hawthorn, J., Tepper-García, T., Agertz, O., & Federrath, C. 2024, *ApJ*, 968, 86
 Bland-Hawthorn, J., Tepper-García, T., Agertz, O., & Freeman, K. 2023, *ApJ*, 947, 80
 Bournaud, F., Dekel, A., Teyssier, R., et al. 2011, *ApJ*, 741, L33
 Bradley, L., Sipocz, B., Robitaille, T., et al. 2016, *Photutils: Photometry tools, Astrophysics Source Code Library, record ascl:1609.011*
 Brammer, G. 2025, *Grizli: Grism Redshift and Line Analysis Software*
 Brammer, G. B., van Dokkum, P. G., Franx, M., et al. 2012, *ApJS*, 200, 13
 Burkert, A., Förster Schreiber, N. M., Genzel, R., et al. 2016, *ApJ*, 826, 214
 Ceverino, D., Dekel, A., & Bournaud, F. 2010, *MNRAS*, 404, 2151
 Chugunov, I. V., Marchuk, A. A., & Mosenkov, A. V. 2025, arXiv e-prints, arXiv:2501.11670
 Cirasuolo, M., McLure, R. J., Dunlop, J. S., et al. 2007, *MNRAS*, 380, 585
 Coe, D., Umetsu, K., Zitrin, A., et al. 2012, *ApJ*, 757, 22
 Conselice, C. J. 2003, *ApJS*, 147, 1
 Conselice, C. J. 2007, in *IAU Symposium, Vol. 235, Galaxy Evolution across the Hubble Time*, ed. F. Combes & J. Palouš, 381–384
 Conselice, C. J., Bershady, M. A., & Jangren, A. 2000, *ApJ*, 529, 886
 Costantin, L., Pérez-González, P. G., Guo, Y., et al. 2023, *Nature*, 623, 499
 Davies, R., Förster Schreiber, N. M., Cresci, G., et al. 2011, *ApJ*, 741, 69
 Davis, M., Guhathakurta, P., Konidakis, N. P., et al. 2007, *ApJ*, 660, L1
 Dekel, A., Zolotov, A., Tweed, D., et al. 2013, *Monthly Notices of the Royal Astronomical Society*, 435
 Dobbs, C. & Baba, J. 2014, *PASA*, 31, e035
 Dobbs, C. L., Theis, C., Pringle, J. E., & Bate, M. R. 2010, *MNRAS*, 403, 625
 D’Onghia, E., Vogelsberger, M., & Hernquist, L. 2013, *ApJ*, 766, 34
 Eisenstein, D. J., Willott, C., Alberts, S., et al. 2023, arXiv e-prints, arXiv:2306.02465
 El-Badry, K., Quataert, E., Wetzel, A., et al. 2018, *Monthly Notices of the Royal Astronomical Society*, 473, 1930
 Elmegreen, D. M. & Elmegreen, B. G. 2014, *ApJ*, 781, 11
 Elmegreen, D. M., Elmegreen, B. G., Ravindranath, S., & Coe, D. A. 2007, *ApJ*, 658, 763
 Erwin, P. 2018, *MNRAS*, 474, 5372

- Espejo Salcedo, J. M., Glazebrook, K., Fisher, D. B., et al. 2025, MNRAS, 536, 1188
- Euclid Collaboration, Huertas-Company, M., Walmsley, M., et al. 2025a, arXiv e-prints, arXiv:2503.15311
- Euclid Collaboration, Walmsley, M., Huertas-Company, M., et al. 2025b, arXiv e-prints, arXiv:2503.15310
- Fall, S. M. & Romanowsky, A. J. 2013, ApJ, 769, L26
- Ferreira, L., Conselice, C. J., Sazonova, E., et al. 2023, ApJ, 955, 94
- Finkelstein, S. L., Bagley, M. B., Ferguson, H. C., et al. 2023, ApJ, 946, L13
- Förster Schreiber, N. M., Genzel, R., Bouché, N., et al. 2009, ApJ, 706, 1364
- Förster Schreiber, N. M., Übler, H., Davies, R. L., et al. 2019, ApJ, 875, 21
- Förster Schreiber, N. M. & Wuyts, S. 2020, ARA&A, 58, 661
- Freeman, P. E., Izbicki, R., Lee, A. B., et al. 2013, MNRAS, 434, 282
- Fujii, M. S., Bédorf, J., Baba, J., & Portegies Zwart, S. 2018, MNRAS, 477, 1451
- Genzel, R., Burkert, A., Bouché, N., et al. 2008, ApJ, 687, 59
- Genzel, R., Förster Schreiber, N. M., Übler, H., et al. 2017, Nature, 543, 397
- Genzel, R., Jolly, J. B., Liu, D., et al. 2023, ApJ, 957, 48
- Genzel, R., Price, S. H., Übler, H., et al. 2020, ApJ, 902, 98
- Genzel, R., Tacconi, L. J., Eisenhauer, F., et al. 2006, Nature, 442, 786
- Giavalisco, M., Ferguson, H. C., Koekemoer, A. M., et al. 2004, ApJ, 600, L93
- Gillman, S., Tiley, A. L., Swinbank, A. M., et al. 2020, MNRAS, 492, 1492
- Grogin, N. A., Kocevski, D. D., Faber, S. M., et al. 2011, ApJS, 197, 35
- Guo, Y., Ferguson, H. C., Bell, E. F., et al. 2015, ApJ, 800, 39
- Guo, Y., Jogee, S., Finkelstein, S. L., et al. 2023, ApJ, 945, L10
- Guo, Y., Jogee, S., Wise, E., et al. 2024, arXiv e-prints, arXiv:2409.06100
- Harrison, C. M., Johnson, H. L., Swinbank, A. M., et al. 2017, MNRAS, 467, 1965
- Hart, R. E., Bamford, S. P., Hayes, W. B., et al. 2017, MNRAS, 472, 2263
- Hart, R. E., Bamford, S. P., Willett, K. W., et al. 2016, MNRAS, 461, 3663
- Huertas-Company, M., Iyer, K. G., Angeloudi, E., et al. 2024, A&A, 685, A48
- Hunter, J. D. 2007, Computing in Science & Engineering, 9, 90
- Jacobs, C., Glazebrook, K., Calabrò, A., et al. 2023, ApJ, 948, L13
- Jogee, S., Barazza, F. D., Rix, H.-W., et al. 2004, ApJ, 615, L105
- Johnson, H. L., Harrison, C. M., Swinbank, A. M., et al. 2018, MNRAS, 474, 5076
- Kartaltepe, J. S., Mozena, M., Kocevski, D., et al. 2015, ApJS, 221, 11
- Kartaltepe, J. S., Rose, C., Vanderhoof, B. N., et al. 2023, ApJ, 946, L15
- Kassin, S. A., Weiner, B. J., Faber, S. M., et al. 2012, ApJ, 758, 106
- Kendall, S., Clarke, C., & Kennicutt, R. C. 2015, MNRAS, 446, 4155
- Koekemoer, A. M., Aussel, H., Calzetti, D., et al. 2007, ApJS, 172, 196
- Koekemoer, A. M., Faber, S. M., Ferguson, H. C., et al. 2011, ApJS, 197, 36
- Kuhn, V., Guo, Y., Martin, A., et al. 2024, ApJ, 968, L15
- Lang, P., Förster Schreiber, N. M., Genzel, R., et al. 2017, ApJ, 840, 92
- Lang, P., Wuyts, S., Somerville, R. S., et al. 2014, ApJ, 788, 11
- Law, D. R., Shapley, A. E., Steidel, C. C., et al. 2012, Nature, 487, 338
- Law, D. R., Steidel, C. C., Erb, D. K., et al. 2009, ApJ, 697, 2057
- Lawrence, A., Warren, S. J., Almaini, O., et al. 2007, MNRAS, 379, 1599
- Le Conte, Z. A., Gadotti, D. A., Ferreira, L., et al. 2024, MNRAS, 530, 1984
- Lee, J. H., Park, C., Hwang, H. S., & Kwon, M. 2024, ApJ, 966, 113
- Lian, J. & Luo, L. 2024, ApJ, 960, L10
- Liang, X., Yu, S.-Y., Fang, T., & Ho, L. C. 2023, arXiv e-prints, arXiv:2311.04019
- Lin, L., Patton, D. R., Koo, D. C., et al. 2008, ApJ, 681, 232
- Liu, Z., Morishita, T., & Kodama, T. 2023, ApJ, 955, 29
- Lotz, J. M., Davis, M., Faber, S. M., et al. 2008, ApJ, 672, 177
- Lotz, J. M., Madau, P., Giavalisco, M., Primack, J., & Ferguson, H. C. 2006, ApJ, 636, 592
- Lotz, J. M., Primack, J., & Madau, P. 2004, AJ, 128, 163
- Madau, P. & Dickinson, M. 2014, ARA&A, 52, 415
- Margalef-Bentabol, B., Conselice, C. J., Haeussler, B., et al. 2022, MNRAS, 511, 1502
- Martorano, M., van der Wel, A., Baes, M., et al. 2025, A&A, 694, A76
- Martorano, M., van der Wel, A., Bell, E. F., et al. 2023, ApJ, 957, 46
- Momcheva, I. G., Brammer, G. B., van Dokkum, P. G., et al. 2016, ApJS, 225, 27
- Morishita, T., Ichikawa, T., & Kajisawa, M. 2014, ApJ, 785, 18
- Nelson, E. J., Suess, K. A., Bezanson, R., et al. 2023, ApJ, 948, L18
- Nestor Shachar, A., Price, S. H., Förster Schreiber, N. M., et al. 2023, ApJ, 944, 78
- Newman, S. F., Genzel, R., Förster Schreiber, N. M., et al. 2013, ApJ, 767, 104
- Noordermeer, E. 2008, MNRAS, 385, 1359
- Obreschkow, D. & Glazebrook, K. 2014, ApJ, 784, 26
- Pandya, V., Zhang, H., Huertas-Company, M., et al. 2024, ApJ, 963, 54
- Peng, C. Y., Ho, L. C., Impey, C. D., & Rix, H.-W. 2002, AJ, 124, 266
- Peng, C. Y., Ho, L. C., Impey, C. D., & Rix, H.-W. 2010, AJ, 139, 2097
- Posti, L., Fraternali, F., Di Teodoro, E. M., & Pezzulli, G. 2018, A&A, 612, L6
- Price, S. H., Kriek, M., Barro, G., et al. 2020, ApJ, 894, 91
- Price, S. H., Kriek, M., Shapley, A. E., et al. 2016, ApJ, 819, 80
- Price, S. H., Shimizu, T. T., Genzel, R., et al. 2021, ApJ, 922, 143
- Ren, J., Liu, F. S., Li, N., et al. 2024, ApJ, 969, 4
- Rodriguez-Gomez, V., Genel, S., Vogelsberger, M., et al. 2015, MNRAS, 449, 49
- Rodriguez-Gomez, V., Snyder, G. F., Lotz, J. M., et al. 2019, MNRAS, 483, 4140
- Scoville, N., Aussel, H., Brusa, M., et al. 2007, ApJS, 172, 1
- Sellwood, J. A. & Carlberg, R. G. 1984, ApJ, 282, 61
- Sellwood, J. A. & Masters, K. L. 2022, ARA&A, 60 [arXiv:2110.05615]
- Sheth, K., Elmegreen, D. M., Elmegreen, B. G., et al. 2008, ApJ, 675, 1141
- Shu, F. H. 2016, ARA&A, 54, 667
- Simons, R. C., Kassin, S. A., Weiner, B. J., et al. 2017, ApJ, 843, 46
- Skelton, R. E., Whitaker, K. E., Momcheva, I. G., et al. 2014, ApJS, 214, 24
- Speagle, J. S., Steinhardt, C. L., Capak, P. L., & Silverman, J. D. 2014, ApJS, 214, 15
- Stott, J. P., Swinbank, A. M., Johnson, H. L., et al. 2016, MNRAS, 457, 1888
- Suess, K. A., Bezanson, R., Nelson, E. J., et al. 2022, ApJ, 937, L33
- Tacconi, L. J., Genzel, R., & Sternberg, A. 2020, ARA&A, 58, 157
- Teklu, A., Remus, R., Dolag, K., et al. 2015, The Astrophysical Journal, 812
- Tiley, A. L., Gillman, S., Cortese, L., et al. 2021, MNRAS, 506, 323
- Tiley, A. L., Swinbank, A. M., Harrison, C. M., et al. 2019, MNRAS, 485, 934
- Tohill, C., Bamford, S. P., Conselice, C. J., et al. 2024, ApJ, 962, 164
- Toomre, A. 1964, ApJ, 139, 1217
- Toomre, A. 1981, in Structure and Evolution of Normal Galaxies, ed. S. M. Fall & D. Lynden-Bell, 111–136
- Toomre, A. & Toomre, J. 1972, ApJ, 178, 623
- Übler, H., Förster Schreiber, N. M., Genzel, R., et al. 2017, ApJ, 842, 121
- Übler, H., Genzel, R., Tacconi, L. J., et al. 2018, ApJ, 854, L24
- Übler, H., Genzel, R., Wisnioski, E., et al. 2019, ApJ, 880, 48
- Umehata, H., Steidel, C. C., Smail, I., et al. 2024, arXiv e-prints, arXiv:2410.22155
- van der Velden, E. 2020, The Journal of Open Source Software, 5, 2004
- van der Walt, S., Colbert, S. C., & Varoquaux, G. 2011, Computing in Science and Engineering, 13, 22
- van der Wel, A., Franx, M., van Dokkum, P. G., et al. 2014, ApJ, 788, 28
- Virtanen, P., Gommers, R., Oliphant, T. E., et al. 2019, arXiv e-prints, arXiv:1907.10121
- Whitaker, K. E., Franx, M., Leja, J., et al. 2014, ApJ, 795, 104
- Wisnioski, E., Förster Schreiber, N. M., Fossati, M., et al. 2019, ApJ, 886, 124
- Wisnioski, E., Förster Schreiber, N. M., Wuyts, S., et al. 2015, ApJ, 799, 209
- Wuyts, S., Förster Schreiber, N. M., Genzel, R., et al. 2012, ApJ, 753, 114
- Wuyts, S., Förster Schreiber, N. M., Lutz, D., et al. 2011a, ApJ, 738, 106
- Wuyts, S., Förster Schreiber, N. M., van der Wel, A., et al. 2011b, ApJ, 742, 96
- Wuyts, S., Förster Schreiber, N. M., Wisnioski, E., et al. 2016, ApJ, 831, 149
- Yao, Y., Song, J., Kong, X., et al. 2023, ApJ, 954, 113
- Yu, S.-Y., Kalinova, V., Colombo, D., et al. 2022, A&A, 666, A175
- Zhang, J., Wuyts, S., Cutler, S. E., et al. 2023, MNRAS, 524, 4128

Appendix A: Observational limitations

Understanding the differences between observed and intrinsic galaxy fractions requires careful consideration of several observational limitations. Key factors include the impact of resolution, which can obscure small-scale morphological features, and cosmological surface brightness dimming, which reduces the visibility of faint structures at higher redshifts. Additionally, the methods used for data analysis, including the choice of morphological indicators and sample selection criteria, play a significant role in shaping the observed fractions. Discrepancies can also arise from inconsistencies in visual classifications and how/whether to translate vote fractions into binary labels, in which subjective biases or differences may influence the classification results. Addressing these limitations is critical for accurately interpreting the observed properties of galaxies and comparing them to their intrinsic characteristics.

Appendix A.1: Resolution and dimming effects

Spatial resolution plays a crucial role in determining the level of detail that can be resolved using *JWST* NIRC*am* images. For *JWST* NIRC*am*, the resolution is limited by the instrument's point spread function (PSF), with a Full Width at Half Maximum (FWHM) of approximately 0.035–0.16 arcseconds, depending on the filter (see Figure 2). At the redshifts of $z = [0.8 - 1.3]$, this corresponds to a physical resolution of approximately 0.28 to 1.29 kpc, while at $z = [2.0 - 2.5]$, it corresponds to 0.29 to 1.32 kpc. This similarity in spatial scale arises from the non-linear relationship between angular diameter distance and redshift, indicating that spatial resolution is not the primary cause of differences between morphological fractions between the two redshift bins.

Cosmological dimming further complicates the detection of galaxy structures. Surface brightness decreases by a factor of $(1+z)^4$, meaning galaxies at higher redshifts appear significantly fainter per unit area. For the mean redshifts of our chosen bins ($z = 1.05$ and $z = 2.25$), this results in a dimming factor of approximately 6.32. This dimming predominantly affects smooth, diffuse components of the galaxies, such as the underlying disk flux. In contrast, brighter and more concentrated substructures, such as bulges and clumps, are less affected and remain detectable. As a result, dimming can lead to an underestimation of disk fractions and an overestimation of irregular fractions in high-redshift bins. This effect is more pronounced for shallower *HST* data, where faint features are more easily lost, compared to the deeper *JWST* data, which provides improved sensitivity to low surface brightness structures.

This study benefits from *JWST*'s resolution and superior sensitivity in the near-infrared compared to previous instruments like *HST*. These advancements mitigate many observational challenges, allowing us to recover more complete morphological information. Nevertheless, even with these improvements, the observed morphological fractions in high-redshift bins must be interpreted with caution. The decreasing redshift trends of the disk, spiral, and bar fractions discussed in §4 are partially shaped by these observational effects and may not fully reflect the intrinsic galaxy populations.

Appendix A.2: Dependence on wavelength

The measured morphology of galaxies is strongly dependent on the wavelength of the imaging data. Redder wavelengths are particularly effective at tracing older stellar populations, revealing

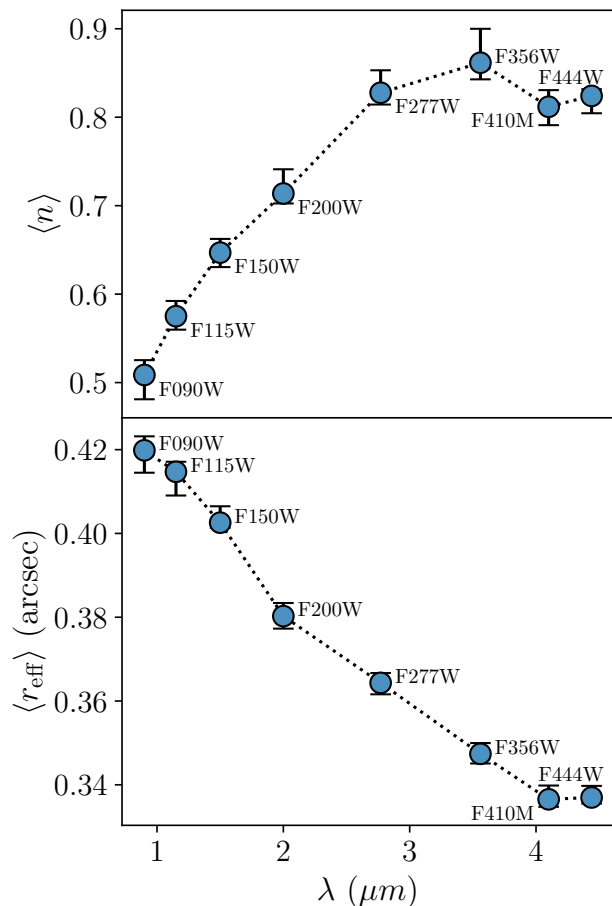


Fig. A.1: Sérsic parameters vs wavelength for the 739 galaxies with the largest combination of filters, which corresponds to 51% of the full sample. The values correspond to the median values in the corresponding wide-band filters and the error bars represent the 68% confidence intervals for the median values, computed using bootstrapped resampling.

prominent structures such as bulges and disks. At these wavelengths, the spatial resolution (≈ 1 kpc) is sufficient to detect large-scale structures, such as bulges and disks, but may obscure smaller-scale features, such as narrow spiral arms or short bars. As a result, classifications of galaxies with compact or subtle morphological components may be biased, potentially overlooking such substructures.

In the context of single-component analysis, commonly used for statistical studies, these biases translate into systematic variations in the inferred Sérsic parameters. To investigate this dependence, we focus on galaxies with NIRC*am* imaging in the most commonly used combination of filters (8 filters): F090W, F115W, F150W, F200W, F277W, F356W, F410M, and F444W. For each filter, we calculate the Sérsic parameters and take the median values across the subset of 743 galaxies, representing 51% of the full sample. The results, shown in Figure A.1, highlight systematic trends. The top panel demonstrates that the Sérsic index (n) increases steadily as the filter wavelength moves from shorter to longer wavelengths. Similarly, the bottom panel shows a corresponding decrease in the effective radius (r_{eff}) with increasing filter wavelength. These trends are also fully consistent with the *HST* vs *JWST* comparison in §D, where the red-

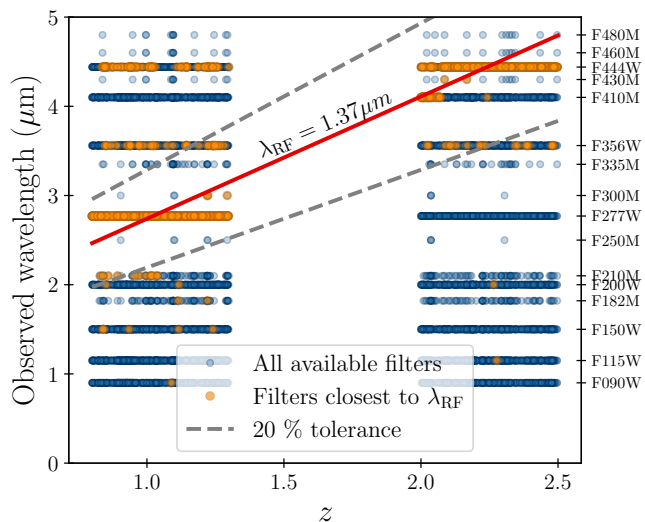


Fig. B.1: The optimal rest-frame wavelength for consistently calculating non-parametric morphological indicators across the sample was determined to be $\lambda_{\text{RF}} = 1.37\mu\text{m}$ (red solid line). Approximately 1,300 galaxies in the sample have imaging in filters corresponding to this rest-frame wavelength, within a 20% margin of error that corresponds to $\pm 0.27\mu\text{m}$ (indicated by the dashed lines). Most galaxies in the low-redshift bin are observed in the F277W filter, while those in the high-redshift bin are predominantly observed in the F444W filter. The plot illustrates the wavelengths of the available filters (blue) and the closest matching filter to λ_{RF} for each galaxy at its respective redshift (orange).

der wavelengths yield systematically larger Sérsic indices and shorter effective radii.

Appendix B: Morphological metrics preparation

We describe below the preparatory steps before running `statmorph`, with the goal of homogenizing the dataset.

Appendix B.1: Wavelength and PSF matching

The quantification of morphological metrics based on unmodified *JWST* data is expected to exhibit redshift-dependent variations. These arise from intrinsic differences in galaxy morphology across redshifts as well as observational effects, which stem primarily from the following:

1. **Rest-Frame Wavelength Shifts:** Variations in rest-frame wavelengths (λ_{RF}) probed by a given filter across the sample imply that different features of galaxy morphology would be highlighted at different redshifts.
2. **Angular Resolution Differences:** Variations in angular diameter distance with redshift affect how the instrument's fixed angular resolution, set by its PSF, translates into the ability to resolve galaxy features.
3. **Cosmological dimming:** Surface brightness decreases with redshift as $(1+z)^4$. For the mean redshift of our chosen redshift bins ($z = 1.05$ and $z = 2.25$), this means a factor of approximately 6.3.

In order to distinguish between intrinsic differences and observational effects, we modified the data to create a uniform

sample, ensuring fair comparisons across galaxies. To minimize rest-frame wavelength differences, we selected the observed wavelength closest to the target rest-frame wavelength ($\lambda_{\text{RF}} = 1.37\mu\text{m}$) for each galaxy, discarding cases where no suitable match within $\pm 20\%$ was available, as illustrated in Figure B.1. To address spatial resolution differences, we convolved the images to a common point spread function (PSF), as shown in Figure B.2. The steps for making the sample uniform are outlined below:

- Filter Selection:* Each galaxy is assigned a specific filter based on the matched rest-frame wavelength ($\lambda_{\text{RF}} = 1.37\mu\text{m}$), with its corresponding PSF.
- Spatial Resolution Calculation:* The spatial resolution for each galaxy is determined by converting the width of its PSF (e.g., FWHM) into physical units (e.g., kpc) at the galaxy's redshift.
- Target PSF Identification:* The galaxy with the lowest spatial resolution (largest physical PSF size) is identified. For our sample, this corresponds to observing an object at $z \approx 2$ with the F444W filter, equivalent to a PSF width in physical units of 1.19 kpc. This becomes the target PSF to which the entire sample is matched.
- PSF Rescaling:* For each galaxy, the target PSF is rescaled to match the pixel scale of that galaxy's image.
- Kernel Creation:* A convolution kernel is generated to transform the PSF of each galaxy to the rescaled target PSF.
- PSF Matching:* The data and PSF of each galaxy are convolved with the kernel to match the spatial resolution to the target PSF. The accuracy of this process is assessed by comparing the resulting PSF to the scaled target PSF.

By accounting for observational effects, the modifications reduce the resolution of the data, resulting in some loss of information. However, this trade-off is essential for minimizing biases towards the lower-redshift objects (e.g., overestimating clumpiness). Additionally, for `STATMORPH` calculations, the adjustments improve reliability by mitigating issues in segmentation and masking, particularly in lower-wavelength images where such calculations are prone to fail. Despite these benefits, it is acknowledged that some previously resolved features may be lost due to the decreased resolution.

Appendix B.2: Segmentation map and masking

The precision of morphological indicator calculations was enhanced by applying masks generated from segmentation maps with brightness thresholds. These thresholds were determined on an image-by-image basis using a custom iterative method. The process involved incrementally lowering the threshold while tracking changes in two parameters: the ratio of the threshold to the mean brightness of the central object and the relative increase in the enclosed area. An approximate outline of this method is illustrated in Figure B.3, while example masking results for selected galaxies are presented in Figure B.4.

Appendix C: Separation Efficiency in Morphological Parameter Spaces

For each pair of morphological indicators provided by `STATMORPH`, we evaluate how effectively mergers can be distinguished from non-mergers, galaxies with bulges from those without bulges, and clumpy galaxies from non-clumpy galaxies within

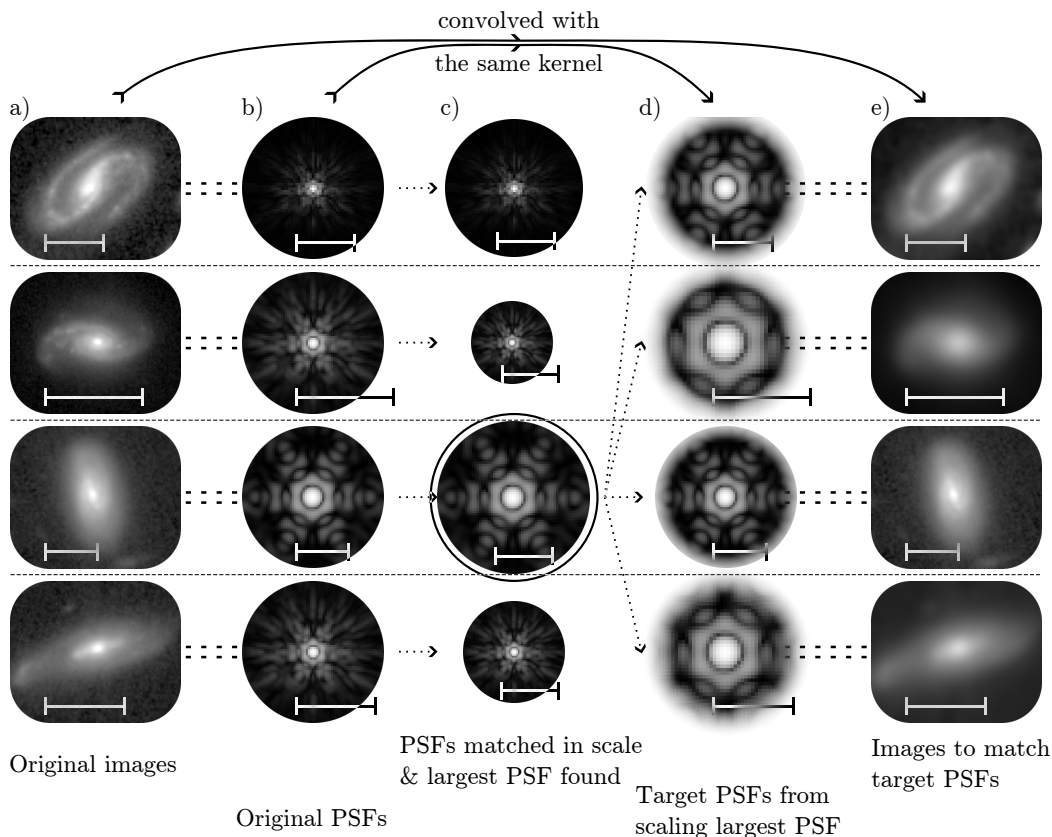


Fig. B.2: Illustration of the method used to match the spatial resolution of galaxy images across the sample, so that all galaxies appear as they would under identical observing conditions. (a) *Original images*: Initial galaxy images, with a 2 kpc horizontal scale bar indicating their physical size at the galaxy’s redshift. (b) *Original PSFs*: The point spread functions (PSFs) corresponding to each image. (c) *Scaling the PSFs*: To enable a fair comparison, PSFs are rescaled to represent physical sizes (kpc) consistently. The FWHM of each PSF is measured, and the galaxy with the largest PSF is identified. In this case, the largest PSF corresponds to a galaxy at $z = 2$ observed with the F444W filter, with a PSF width of 1.19 kpc. (d) *Creating target PSFs*: The largest PSF from (c) is used as a reference. It is rescaled to match each galaxy’s physical size while maintaining a constant FWHM in spatial units. This ensures that all PSFs correspond to the same physical resolution across the sample. This is evident in the main PSF component, which spans a fixed fraction (approximately half) of the horizontal scale bar across all images. (e) *Final image matching*: Each original image (from panel a) is convolved with a kernel derived from the rescaled PSFs (panel d). This convolution results in a final set of images that all share the same spatial resolution, making them directly comparable.

their respective parameter spaces. This is done by iteratively determining an optimal linear boundary that minimizes contamination on both sides.

We define contamination as the total fraction of misclassified objects across all categories. It is computed as the sum of misclassification rates where one corresponds to the fraction of objects that belong to a category but were not classified as such (false negatives rate), and the other one is the fraction of objects incorrectly assigned to that category (false positives rate). The summed misclassification rates provide a simple measure of the overall contamination. Table C.1 illustrates the parameters used in this calculation, where the contamination C is defined as

$$C = \frac{a}{a+b} + \frac{c}{c+d}. \quad (\text{C.1})$$

The separation efficiency of a given parameter space is directly linked to contamination, defined as $1 - C_{\min}$, where C_{\min} is the lowest contamination achievable within that space by any dividing line. The full separation efficiency results for galaxies

	Reference	
Classified	In category	Not in category
In category	b	a
Not in category	c	d

Table C.1: Definition of parameters used in the contamination calculations. Rows indicate the visual category assigned to each object, while columns refer to the reference category, i.e. the morphological category against which contamination is evaluated. The entries denote the number of galaxies in each combination: a and c are misclassifications, with a representing objects incorrectly classified as belonging to the given category, and c representing objects that should have been classified as such but were not. The letters b and d are correct classifications. Contamination is computed as the sum of misclassification rates, as defined in Equation C.1.

with and without bulges, mergers and non-mergers and clumpy

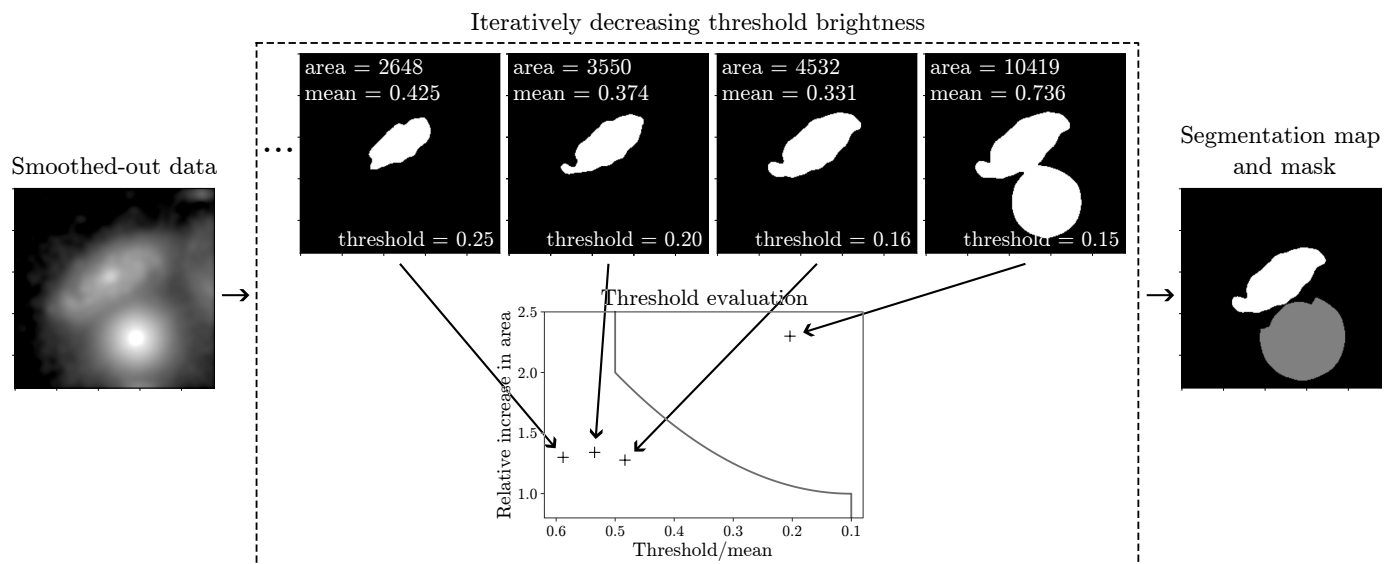


Fig. B.3: Illustration of the iterative process used to determine the brightness threshold for constructing the segmentation map. We start by smoothing out the image data with a 10-pixel-wide Gaussian. Then at each step, the brightness threshold is decreased incrementally, and the impact is assessed by examining (1) the relative increase in the area enclosed by the threshold (y-axis) and (2) the ratio of the threshold value to the mean brightness within the enclosed area (x-axis). The threshold is deemed sufficiently low when the target object can be distinguished from other objects in the image, which is determined by whether the cutoff curve (grey) has been crossed in this parameter space. The optimal shape of the cutoff curve was established through manual evaluation of a randomly selected subset of the sample.

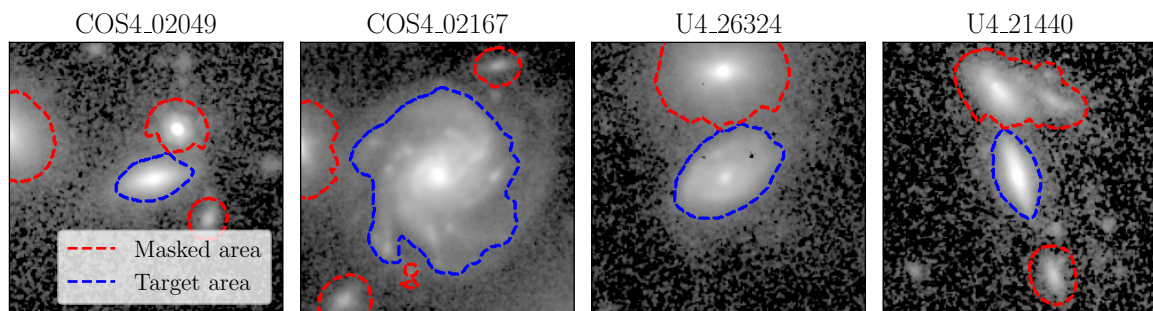


Fig. B.4: Four examples of the masking applied during data preparation prior to the STATMORPH analysis. Red dashed lines indicate the masked areas and blue dashed lines correspond to the target segmentation maps. The brightness threshold used to define both areas was determined through the iterative process illustrated in Figure B.3.

and non-clumpy galaxies are presented in Tables C.2, C.3, C.4, respectively.

As an illustrative example, in the case of clumpy galaxies and for the Gini vs A combination, the minimal contamination corresponds to $C_{\min} = \frac{25}{25+112} + \frac{389}{389+695} = 0.54$, and thus the separation efficiency corresponds to $1 - C_{\min} = 0.46$. The line of best separation that optimizes this separation efficiency is shown in the right panel of Figure 13.

Appendix D: Comparisons with *HST* photometry

The *JWST* data extend the wavelength range for morphological studies beyond what is accessible with *HST*, enabling rest-frame near-infrared coverage up to $2 \mu\text{m}$ for $0.8 < z < 1.3$ and up to $1.5 \mu\text{m}$ for $2.0 < z < 2.5$ (see Figure D.1 for a comparison). This extended range reveals the bulk of the underlying stellar mass distribution which was dust-attenuated (e.g., Martorano et al. (2023) and Huertas-Company et al. (2024)). In con-

trast, *HST*'s photometry, limited to shorter wavelengths, is more sensitive to dust and star-forming regions, often leading to underestimation of bulge prominence and overemphasis of clumpy features. Moreover, beyond its improved wavelength coverage, *JWST*'s higher sensitivity enables the detection of faint extended emission, further enhancing the ability to resolve galaxy structures in greater detail.

To explore these differences in practice, we compare the Sérsic best-fit parameters estimated with STATMORPH from both *JWST* and *HST* images. Specifically, for a wavelength-independent comparison, we analyze galaxies in *JWST* F150W vs. *HST* F160W. And to assess wavelength-dependent effects, we compare *JWST* F444W vs. *HST* F160W. All the calculations followed the same methodology with STATMORPH for a fully consistent comparison. Both comparisons are shown in Figure D.2.

- *Sérsic Index*: When comparing the same wavelength (*JWST* F150W vs. *HST* F160W), the Sérsic index remains consis-

Table C.2: Separation efficiency of galaxies with and without bulges across parameter spaces defined by various morphological indicators. The values represent the effectiveness of each parameter combination, with higher values indicating better separation. The combination of Gini and M_{20} provides a prominent separation of bulges and non-bulges, consistent with its frequent use in morphological studies. M_{20} alone also demonstrates strong discriminatory power. Additionally, the combination of r_{eff} and intensity-based statistics performs comparably to the Gini and M_{20} indicators.

	Gini	M_{20}	C	A	S	M	I	D	n	r_{eff}
Gini	0.034	0.453	0.311	0.119	0.213	0.157	0.185	0.255	0.242	0.223
M_{20}		0.388	0.422	0.422	0.397	0.397	0.393	0.412	0.459	0.456
C			0.177	0.179	0.238	0.213	0.189	0.275	0.208	0.275
A				0.111	0.219	0.192	0.165	0.311	0.194	0.312
S					0.208	0.238	0.232	0.305	0.240	0.302
M						0.153	0.185	0.258	0.205	0.353
I							0.153	0.260	0.192	0.379
D								0.246	0.275	0.366
n									0.191	0.265
r_{eff}										0.205

Table C.3: Similar to Table C.2, but for mergers and non-mergers.

	Gini	M_{20}	C	A	S	M	I	D	n	r_{eff}
Gini	0.132	0.530	0.288	0.570	0.244	0.500	0.521	0.517	0.405	0.206
M_{20}		0.445	0.541	0.553	0.450	0.536	0.534	0.508	0.473	0.466
C			0.160	0.566	0.212	0.500	0.515	0.529	0.265	0.169
A				0.549	0.549	0.571	0.549	0.563	0.549	0.549
S					0.200	0.508	0.513	0.515	0.281	0.233
M						0.500	0.533	0.545	0.506	0.521
I							0.510	0.557	0.517	0.523
D								0.505	0.518	0.508
n									0.261	0.261
r_{eff}										0.160

Table C.4: Similar to Table C.2, but for clumpy and non-clumpy galaxies.

	Gini	M_{20}	C	A	S	M	I	D	n	r_{eff}
Gini	0.403	0.431	0.431	0.459	0.433	0.409	0.413	0.432	0.411	0.420
M_{20}		0.123	0.315	0.375	0.164	0.252	0.292	0.141	0.314	0.338
C			0.261	0.399	0.278	0.300	0.354	0.272	0.309	0.389
A				0.355	0.356	0.364	0.359	0.387	0.369	0.366
S					0.126	0.252	0.275	0.147	0.310	0.326
M						0.252	0.299	0.255	0.303	0.329
I							0.271	0.312	0.343	0.323
D								0.101	0.340	0.338
n									0.301	0.387
r_{eff}										0.322

tent. However, for *JWST* F444W vs. *HST* F160W, we observe a mild systematic increase in n , consistent with previous findings (Martorano et al. 2025) showing higher near-IR Sérsic indices for massive galaxies ($\log(M_{\star}/M_{\odot}) > 10.5$). This increase may reflect differences in stellar population gradients and dust attenuation, which are less prominent at longer wavelengths.

- *Effective Radius*: While size measurements are consistent at matched wavelengths, galaxies appear systematically smaller in *JWST* F444W compared to *HST* F160W. This trend aligns with Suss et al. (2022), who found that near-IR galaxy sizes tend to be smaller due to radial M/L ratio variations driven by dust attenuation and stellar age gradients (e.g., Wuyts et al. 2012, Zhang et al. 2023).

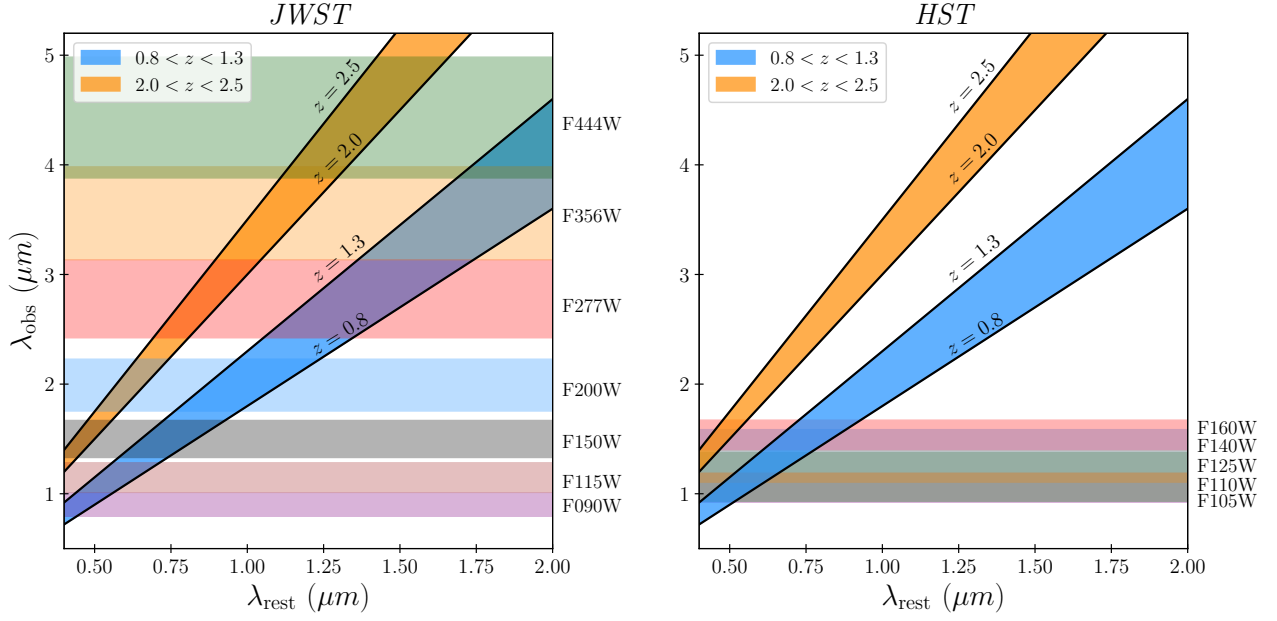


Fig. D.1: Comparison of the broad-band filter coverage of *JWST* (left) and *HST* (right) for the two redshift bins used in this study. The extended wavelength coverage of *JWST* enables us to probe rest-frame wavelengths up to $2 \mu\text{m}$ for the low-redshift bin and up to $1.5 \mu\text{m}$ for the high-redshift bin, providing new insights into the morphologies of these systems.

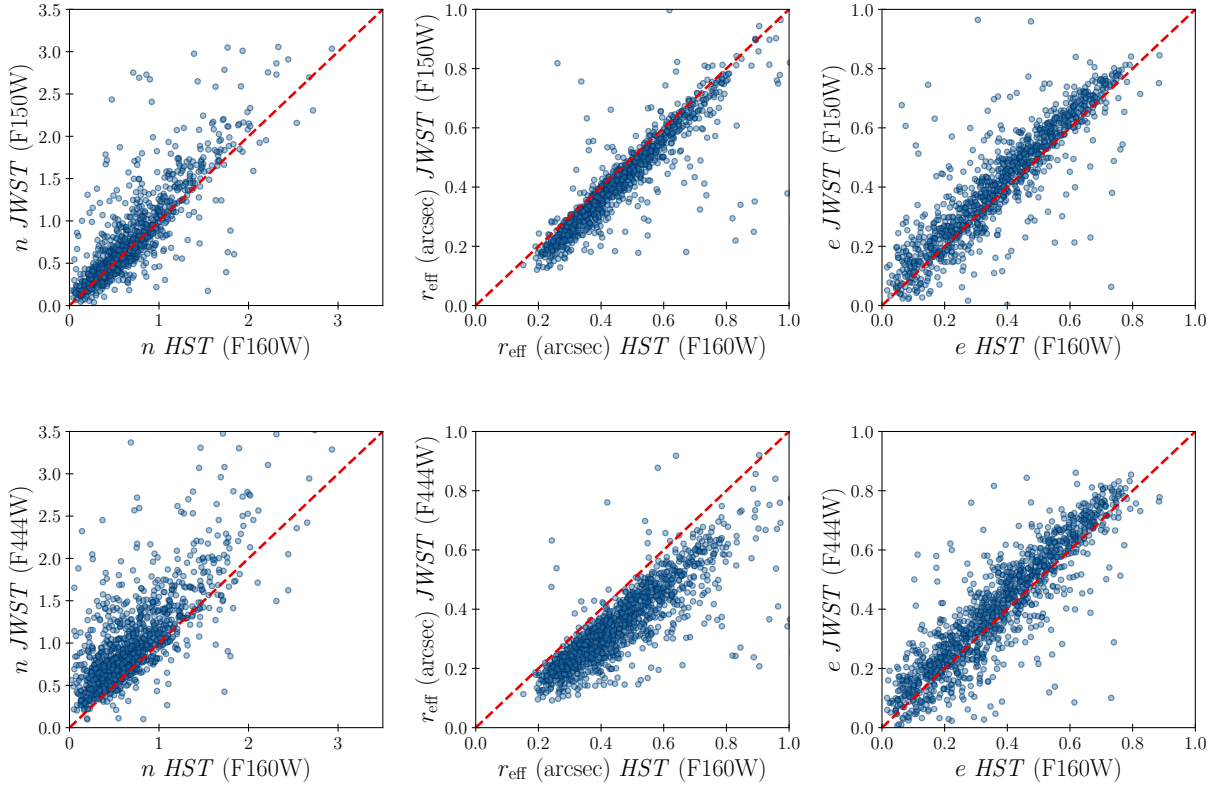


Fig. D.2: Comparison of Sérsic profile parameters measured from *JWST* and *HST* imaging using `statmorph`. The top row compares *JWST* F150W with *HST* F160W, while the bottom row compares *JWST* F444W with *HST* F160W. From left to right, each panel shows the Sérsic index (n), effective radius (r_{eff}), and ellipticity (e). The red dashed line represents the one-to-one relation. Sérsic indices show overall agreement at matched wavelengths, but higher values in *JWST* F444W, consistent with expectations from stellar population gradients and dust attenuation effects. Effective radii remain similar at matched wavelengths but appear systematically smaller in F444W, consistent with radial mass-to-light ratio variations. Ellipticities show strong agreement across all bands, with minor scatter.